Kinematic Earthquake Source Inversion and Tsunami Runup Prediction with Regional Geophysical Data

D. Melgar,[1,2] and Y. Bock[1]

Corresponding author: D. Melgar, Seismological Laboratory, University of California Berkeley 215 McCone Hall #4760 Berkeley, CA 94720-4760, USA. (dmelgar@berkeley.edu)

[1]Cecil H. and Ida M. Green Institute of Geophysics and Planetary Physics, Scripps Institution of Oceanography, University of California San Diego, La Jolla, California, USA.

[2]Now at Seismological Laboratory, University of California Berkeley, Berkeley, California, USA.

This article has been accepted for publication and undergone full peer review but has not been through the copyediting, typesetting, pagination and proofreading process, which may lead to differences between this version and the Version of Record. Please cite this article as doi: 10.1002/2014JB011832

Abstract. Rapid near-source earthquake source modeling relying only on strong motion data is limited by instrumental offsets and magnitude saturation, adversely affecting subsequent tsunami prediction. Seismogeodetic displacement and velocity waveforms estimated from an optimal combination of high-rate GPS and strong motion data overcome these limitations. Supplementing land-based data with offshore wave measurements by seafloor pressure sensors and GPS-equipped buoys can further improve the image of the earthquake source and prediction of tsunami extent, inundation and runup. We present a kinematic source model obtained from a retrospective real-time analysis of a heterogeneous data set for the 2011 M_w 9.0 Tohoku-oki, Japan earthquake. Our model is consistent with conceptual models of subduction zones, exhibiting depth dependent behavior that is quantified through frequency domain analysis of slip rate functions. The stress drop distribution is found to be significantly more correlated with aftershock locations and mechanism types when off-shore data are included. The kinematic model parameters are then used as initial conditions in a fully non-linear tsunami propagation analysis. Notably, we include the horizontal advection of steeply sloping bathymetric features. Comparison with post-event on-land survey measurements demonstrates that the tsunami's inundation and runup are predicted with considerable accuracy, only limited in scale by the resolution of available topography and bathymetry. We conclude that it is possible to produce credible and rapid, kinematic source models and tsunami predictions within minutes of earthquake onset time for near-source coastal regions most

susceptible to loss of life and damage to critical infrastructure, regardless of earthquake magnitude.

1. Background

Mitigation of the effects of natural hazards on public safety and civilian infrastructure is a multidisciplinary problem. It includes both the societal aspects of how we respond to hazards and the physics behind these phenomena. As we seek to gain knowledge about Earth processes we must also consider the practical implications of the research. The number of people and infrastructure located in areas of earthquake and tsunami hazard is constantly growing. The problem of mitigating risk can be confronted from three perspectives. One is to minimize the hazard by moving people and infrastructure away from earthquake and tsunami-prone areas or limiting development in those areas. This is impractical for densely populated areas or already existing population concentrations. The second approach is to minimize vulnerability by making infrastructure more resilient to the effects of natural hazards and educating the public prior to a disaster. The third approach and the focus of this study is to provide early warnings and rapid actionable information, specifically for earthquakes with tsunamigenic potential.

1.1. Seismic-Based Systems

Several countries operate some form of earthquake early warning and rapid response system [*Allen et al.*, 2009]; the systems in Japan and Mexico, have been operational for over 20 years. Philosophies on how to approach this problem vary and are mostly contingent on the type of hazard the system is planned for (subduction zone vs. transform boundary events) and whether the system is designed to alert the population or to protect infrastructure by stopping trains or shutting down power plants, for example. Whichever strategy is employed, earthquake early warning systems rely on traditional seismic sen-

sors, seismometers and accelerometers. It has been observed that these systems suffer from a condition known as saturation [*Brown et al.*, 2011] where at large magnitudes it becomes increasingly difficult to separate one earthquake from another. Indeed, during the 2011 M_w9 Tohoku-oki, Japan event the initial magnitude estimates never exceeded M_w8 [*Hoshiba and Ozaki*, 2014]. There is debate in the literature as to whether this is due to the physics of the source or if it is an instrumental issue. Related is whether an earthquake is deterministic and its magnitude is determined in the first seconds of rupture initiation [*Olson and Allen*, 2005; *Rydelek and Horiuchi*, 2006].

It is well known that as magnitude increases the spectrum of seismic radiation will become enriched in long period energy [*Haskell*, 1964; *Brune*, 1970] so it is tantalizing to consider that perhaps the saturation problem is instrumental rather than physical. At local distances from large earthquakes, where saturation occurs in early warning scaling laws, seismologists must rely on strong motion sensors whose low gains permit the instrument to stay on scale during shaking. These sensors, however, are affected by systematic errors such as un-modeled rotational motions [*Trifunac and Todorovska*, 2001] that render the long period part of the spectrum, at periods roughly longer than 10 s [*Melgar et al.*, 2013a] difficult, if not impossible, to reliably use in real time or without adhoc corrections [*Boore and Bommer*, 2005]. *Crowell et al.* [2013] has shown, albeit with a limited data set, that incorporating Global Positioning Sytem (GPS) data, that can directly measure long period motions into traditional early warning scaling laws appears to ameliorate the saturation problem.

The reliability of long-period strong motion data is a key question for early warning and response. For some applications, simple characterization of the earthquake suffices, only

a rough location and estimate of magnitude or of expected shaking intensity is necessary to trigger an alert. However, immediately following rupture more elaborate models of the source are necessary to guide rapid response. For example the United States Geological Survey's (USGS) Shakemap [*Wald et al.*, 1999] and PAGER [*Jaiswal and Wald*, 2010] applications provide a rapid assessment of expected shaking throughout the epicentral area and indications of where damage to infrastructure and casualties is most severe. The first iterations of these data products rely on simple point source models. They are often revised hours after the event when more complex source models become available. Considering a point source vs. a finite extent source model can have a significant impact in the Shakemap computation [*Colombelli et al.*, 2013]. However, rapid estimates of rupture extent, if they rely on seismic data alone, are delayed due to the aforementioned dificulties in estimating long period ground motions.

1.2. Data Diversity: GPS and Tsunami Wave Measurements

GPS provides a solution to the problem of long period ground motion observation. In particular using the permanent deformation (the static field) measured for an earthquake it is possible to construct models that range from point source [*Melgar et al.*, 2012] to line source moment tensors [*Melgar et al.*, 2013b] and heterogenous slip inversions [*Crowell et al.*, 2012; *Melgar et al.*, 2013b; *Minson et al.*, 2014].

If high-rate GPS (typically 1-5 Hz sampled) and strong motion sensors (100-200 Hz) are collocated they can be used to produce a reliable broadband measurement of strong motion displacement and velocity at the sampling rate of the accelerometer [*Emore et al.*, 2007; *Smyth and Wu*, 2007; *Bock et al.*, 2011]. Such *seismogeodetic* solutions produce

estimates of ground motion reliable from the zero frequency to the Nyquist frequency of the strong motion sensor [*Melgar et al.*, 2013b].

The static field from GPS is the longest period information that is measurable from an earthquake, effectively nullifying any saturation concerns. However, a more complete description of the earthquake source should include the time dependent behavior of rupture, which is typically modeled using seismic accelerations and velocities. Due to the unreliability of strong motion sensors at low frequencies, automated kinematic slip inversions are typically computed with teleseismic data [*Ji et al.*, 2002] and are only available hours after the event [*Hayes et al.*, 2011]. With an example application to the 2011 M_w9 Tohoku-oki we will demonstrate how seismogeodetic data can be used to compute kinematic models of the source. With the combination of local and regional GPS and strong motion recordings these models could be available within minutes of rupture initiation. Data diversity can help to overcome difficulties in source imaging that arise when using only one kind of data set. For example, it has been shown that tsunami waveforms can be used, like their seismic counterparts, for kinematic source inversion [*Fujii and Satake*, 2013; *Satake et al.*, 2013], and they have also been jointly inverted with land-based data to produce static models [*Romano et al.*, 2012; *Melgar and Bock*, 2013]. We show that off-shore tsunami wave measurements when inverted jointly with the land-based seismogeodetic data significantly improve resolution of the shallow portion of the megathrust. The source model thus derived is broadband in the sense that it captures higher frequency detail of rupture at depth which consists of short, sharp slip pulses as well as the long and smooth shallow source time functions. At higher frequencies the joint tsunami and seismogeodetic solution is largely in agreement with teleseismic slip inversions and back projection studies. There

is depth-dependent behavior of rupture as evidenced by analysis of the frequency domain properties of the sub-fault source time functions that agrees with conceptual models of subduction zones [*Lay et al.*, 2012]. Furthermore we find that stress-drop computations from the joint model correlates well with the observed distribution and faulting type of aftershocks following the mainshock.

1.3. Impact on Tsunami Modeling

Importantly, the choice of whether to apply static and kinematic source models can also have a significant impact in tsunami early warning. The tsunami warning centers (TWCs) operated by the National Oceanographic and Atmospheric Administration (NOAA) utilize teleseismic and ocean bottom pressure measurements from DART buoys in the deep ocean. TWCs routinely provided basin-scale warnings in the hours following a large event [*González et al.*, 2005; *Titov et al.*, 2005; *Mungov et al.*, 2013]. The reliance on sensors in the far field of the tsunami source precludes early warning in the near-source region where losses are most severe. Japan operates a system designed to provide near-source warnings [*Tatehata*, 1997; *Ozaki*, 2011]. It utilizes rapidly determined hypocenters and magnitudes from the Japanese Meteorologcal Agency (JMA) to perform a database query of pre-computed scenarios. These scenarios, computed offline and well in advance of the event, include intensity estimates at predetermined locations along the near-shore coast. Thus, when the earthquake strikes these parameters seed the database query and the resulting model guides the warnings issued to the public. During the 2011 M_w9 Tohoku-oki event however, a strict reliance on seismic data for estimation of the earthquake source parameters led to a severe underestimation of magnitude [*Hoshiba and Ozaki*, 2014], once again, due to saturation. This led to underestimates of the extent and intensity of the tsunami,

which were not revised until many hours after the event. We will discuss the utility of kinematic source models for the tsunami warning problem with and without land-based seismogeodetic data and off-shore wave measurements. In *Melgar and Bock* [2013] we demonstrated an indirect approach to tsunami warning using a static source model. We extend it here to a kinematic source model, which is used to derive the deformation of the seafloor. This is then input along with detailed topographic and bathymetric maps to a fully non-linear tsunami wave propagation analysis using the open-source code GeoClaw [*LeVeque et al.*, 2011] to make a detailed tsunami prediction. Tsunami survey data collected immediately after the 2011 Tohoku-oki event [*Mori et al.*, 2012] allows to assess the accuracy and spatial resolution of a hierarchy of tsunami prediction models. This indirect approach has received renewed attention from the hazards community [*Melgar and Bock*, 2013; *Tsushima et al.*, 2014; *Gusman et al.*, 2014] but the importance of the kinematic earthquake source has been disregarded in these studies. We demonstrate that the source model from land-based seismogeodetic waveforms produces acceptable predictions of tsunami intensity but that the addition of ocean-based observations, produces the most accurate forecast of the tsunami. Thus, with existing geophysical infrastructure it is reasonable to expect detailed tsunami warnings in the coastal immediately adjacent to large events without regard for magnitude or faulting type.

2. Data and Methods

2.1. Data Processing

Strong motion data are unreliable at long periods, while GPS data faithfully record low frequency ground motions. GPS data, however, have lower sensitivity and lower sampling rates, which result in elevated noise levels at higher frequencies [*Genrich and Bock*, 2006].

Thus, when employing either of these data types for slip inversion it is common to high-pass filter the strong motions [*Suzuki et al.*, 2011] and low pass filter the GPS data [*Yue and Lay*, 2011]. This poses a number of challenges for automated and rapid response. The frequency band at which either of the data sets is useful will change from earthquake to earthquake and from site to site. A filter with a certain corner frequency may successfully remove biased data at one site but not at another. Therefore, careful correction and selection of the filter corners is necessary. *Melgar et al.* [2013a] analyzed 48 collocated GPS and strong motion sites that recorded ground motion during the 2011 M_w 9 Tohoku-oki earthquake and found significant differences for the bandwidth at which each site and sensor was reliable. Similar observations were made for a smaller data set for the 2010 M_w 7.2 El Mayor-Cucapah earthquake [*Bock et al.*, 2011]. Thus, for automated and objective correction to both GPS and strong motion data another approach is required. If the two sensors are collocated they can be optimally combined with a Kalman filter [*Bock et al.*, 2011] such that the frequency domain biases of each sensor are mitigated [*Melgar et al.*, 2013a]. In the absence of motion most accelerometers have a small "DC" bias. It is typically accounted for by a zeroth-order correction [*Boore et al.*, 2002]. However, this is difficult to do in a real-time environment required for rapid earthquake response. In this study we employ an augmented form of the Kalman filter that includes an additional state variable that, in addition to displacement and velocity, also estimates this bias [*Melgar*, 2014].

Displacement based inversions, especially when large coseismic offsets are present, will preferentially fit long period data only and produce smooth models [*Yue and Lay*, 2011] while velocity based inversions will provide higher frequency information. In order to ob-

tain a model that is suitable across as broad a frequency range as possible we demonstrate that both displacement and velocity waveforms should be considered. For this study of the 2011 M_w9 Tohoku-oki earthquake we select 20 land-based seismogeodetic stations and include the 3-component displacements and velocities for a total of 120 waveforms (Figure 1).The stations are selected to provide adequate coverage of the rupture area while also taking into account the local site conditions. Many of the GPS/accelerometer pairs belong to the Knet strong motion network, which can have significant site response [*Tsuda et al.*, 2006]. We choose accelerometers at stations with acceptable site conditions by examining their corresponding soil profile maps (http://www.kyoshin.bosai.go.jp/). The offshore data consist of 6 moored GPS buoys (labeled BY) in 125-205m water depths and 2 ocean bottom pressure sensors (labeled OB) in 1000-1600m water depths (Figure 1). Both record transient changes in the sea-surface height. Tides are removed from the data and they are resampled to a 15s sampling rate. There exist numerous tide-gauges in the near-source region and indeed they have been used for tsunami-only inversion [*Satake et al.*, 2013] and static inversion [*Melgar and Bock*, 2013]. However, while the tsunami propagation code we use (GeoClaw) models non-linear tsunami propagation, the assumption of linearity and superposition necessary for inversion is not satisfied in the very shallow water depths of the tide gauges [*Melgar and Bock*, 2013]; therefore, we have disregarded them in this study.

2.2. Slip Inversion

If the timing, magnitude, orientation and geographical location of slip are unknown then inversion for the time-dependent features of the earthquake source is an intractable problem. To turn the slip inversion into a well posed problem, it is typical to assume

a dislocation surface and some parameterization for the shape of the slip rate function, for example, based on crack dynamics [*Beroza and Spudich*, 1988; *Ji et al.*, 2003]. The inverse problem can then be solved non-linearly, with only the timing and amount of slip as unknown. The inversion is rendered linear if the timing of slip is prescribed [*Trifunac*, 1974; *Hartzell and Heaton*, 1983]. The non-linear approach solves directly for rupture velocity but requires simple source-time function parametrizations that might not model source complexities. We follow the linear multi-time window approach [*Ide et al.*, 1996] that can accomodate variable rupture velocity if sub-faults are allowed to slip over multiple intervals. Unlike the non-linear approach, this can yield complex source time functions.

We discretize the 3D slab model of *Hayes et al.* [2012] into 189 25x25km sub faults. The model parameters are twenty 10 second long 50% overlapping triangle source time functions at each subfault. This choice of rise time is rather arbitrary and is perhaps the most ad hoc parameter in the process. However, a rise time of 10s allows for the rupture front to traverse the subfault at a sensible velocity and is in broad agreement with the source-time function scaling laws of *Tanioka and Ruff* [1997]. Maximum allowed rupture velocity is 3.5km/s which corresponds to 80% of the shear wave speed of the deepest layered spanned by the slab model, although choosing a larger value, say, 4km/s has little effect on the inversion. This parameterization allows each subfault to slip for a total of 105s. Note that this does not mean that rupture speed is forced to 0.8 times the shear wave speed, rather that this is the fastest possible rupture velocity allowed in the model.

For the elastic wave portion of the inversion, synthetics are computed with a 1D layered model calibrated for Japan. The model is used for automated computation of CMTs with long period data [*Fukuyama et al.*, 1998; *Tsuruoka et al.*, 2009]. The Green's functions

(GFs) calculation uses the frequency wavenumber integration code provided by *Zhu and Rivera* [2002]. GFs are computed for every subfault/station pair from 0 to 0.5Hz. The 3-component Kalman filtered strong motion displacement and velocity data from the 20 sites are lowpass filtered to 0.5Hz with a zero-phase 8 pole Butterworth filter to match the GFs. For the joint inversion with the tsunami wave gauges, GFs are computed in a two-step process similar to what was outlined in *Melgar and Bock* [2013]. For each subfault we calculate the deformation of the seafloor in the model domain that results from placing 1m of strike-slip and 1m of dip-slip motion on it. We then use the 3D deformation field as the initial condition for tsunami modeling with the GeoClaw software and collect time series of sea surface disturbances at the 8 tsunami wave gauges (Figure 1) sampled at 15s, which are taken as the tsunami GFs (tGFs). This assumes that these tsunami Green's functions (tGFs) can be linearly superimposed. This assumption was tested numerically in *Melgar and Bock* [2013] and was found to be suitable for the deep-water wave gauges. The land-based data and tsunami time series are assigned equal weights.

For regularization we employ a Laplacian smoothness constraint on the total slip at each subfault and a finite difference derivative constraint on the amplitude of the time windows at each subfault. This means we have two smoothing parameters that need to be defined, one temporal and one spatial. We use the formalism of Akaike's Bayesian Information Criterion (ABIC) to decide on the optimal value of the smoothing parameter pair [*Akaike*, 1980; *Fukahata et al.*, 2003]. This minimizes human decision making by providing an objective way for determination of the regularization parameters. Multiple inversions are run to determine the optimum value of the ABIC. In the first iteration 64 inversions are run at a coarse discretization of the regularization parameters. We then

we refine twice around the minimum value of the ABIC to find the optimal inversion (Figure S1); a total of 100 inversions are utilized to determine the optimum regularization parameters.

2.3. Runup Modeling

For simulation of tsunami wave propagation we use the open-source code GeoClaw (http://clawpack.org) by which two-dimensional shallow water equations are solved with the finite volume technique [*LeVeque*, 2002]. GeoClaw has been benchmarked by the National Tsunami Hazard Mitigation Program (NTHMP) [*Gonzalez et al.*, 2011] and approved for use in hazard modeling products.The code simulates non-linear water wave propagation (but is non-dispersive) and can deal with discontinuities in the solution, such as turbulent bore formation, by shock capturing. It employs adaptive mesh refinement (AMR) such that regions of larger tsunami complexity are automatically refined to higher discretization levels according to heuristics prescribed by the user. The code is suitable for near-shore runup analysis. It employs a Manning-type law for bottom friction (we held the coefficient fixed at 0.025), has a moving sea/land boundary condition that allows cells to be wetted or dried as the simulation progresses, and has a non-reflecting outflow boundary condition at the edges of the model domain [*George and LeVeque*, 2006; *George*, 2008; *Berger et al.*, 2011]. For the simulations we use the best publicly available topography and bathymetry data sets. Onshore topography are 90m pixels from the SRTM3 dataset [*Farr et al.*, 2007] and bathymetry are 1km pixels from the SRTM30+ data-set [*Sandwell and Smith*, 2009]. The initial condition for a model run is the sea-floor deformation which we derive from the kinematic inversion. We discretize the model domain into 0.05° by 0.05° nodes and forward compute the 3D motion at each node predicted by

the slip model at 1 second intervals. We then compute the effective vertical deformation $\Delta h(x, y)$ of the 3D surface that describes the ocean bottom $h(x, y)$ at each node and every epoch. Typically, only the vertical deformation is considered in the tsunami initial condition, however, advection of steeply sloping bathymetric features can be a significant tsunamigenic contributor [*Tanioka and Sataka*, 1996]. Thus, the total deformation is the sum of the vertical motion $\Delta z(x, y)$ and the a pseudo-vertical component introduced by the advection of topography $c_x(x, y)$ and $c_y(x, y)$ in both horizontal directions such that:

$$\Delta h(x, y) = \Delta z(x, y) - c_x(x, y)\frac{dh(x, y)}{dx} - c_y(x, y)\frac{dh(x, y)}{dy} \ . \tag{1}$$

This is schematically shown in Figure 2. Note the negative signs in front of the directional derivatives. These indicate that the downward sloping feature west of the trench axis (negative derivative) moving in the positive x direction should cause uplift, as should the upwards sloping feature east of the trench axis moving in the negative x direction. This differs from the purely vertical initial condition where $\Delta h(x, y) = \Delta z(x, y)$. These adjustments are considered in generating the kinematic Green's functions as well as the runup models that follow. The horizontal contribution is sometimes called the *topography effect* [*Bletery et al.*, 2014]. To further illustrate its importance consider Figure 3 where we show the directional derivative of the SRTM30+ bathymetry computed along the average trench-normal direction. The red colors indicate that positive horizontal motion causes uplift, while the blue ones that positive motion causes apparent subsidence. Along the frontal part of the continental slope and close to the trench the values of the derivative are as high as 0.3; the values are also high along the seamounts south of 37°N. This means that for every meter of horizontal motion, 0.3m of apparent vertical motion will

be generated. Clearly, this is not a signal that should be ignored. Once this computation is complete we have obtained effective vertical deformation at all points in the domain for every epoch. We run the simulation forward in time for a total of two hours of model time. For the open ocean we compute snapshots of propagation at 15s intervals and use them to compute the maximum amplitude maps. Additionally, we collect model output at regular points along the coastline as well as at the locations of 2250 post-event survey points of tsunami runup levels. [*Mori et al.*, 2012].

3. Results

3.1. Land-based Inversion

Figure S1 shows the values of the ABIC for 100 inversions with different levels of regularization. As discussed, we select the preferred values of spatial and temporal regularization from the global minimum shown in the figure. The total slip from this preferred joint kinematic inversion, which includes only on-shore seismogeodetic velocity and displacement data (the DV model henceforth), is shown in Figure 4a and has a peak slip value of 52m on the shallowest subfault. Large slip, in excess of 20m occurs on an asperity of about 300x150km up dip of the hypocenter at depths shallower than 20km. Slip at depth tapers off quickly but there is a large area of roughly 200x100km with more than 5-20m of slip extending from a depth of about 50km up dip to the hypocenter. Figure 4b is the source time function for the DV model. Moment rate begins very slowly between 0 and 20s but increases sharply to its peak at 75s. Afterwards it decreases smoothly; the total duration of moment release is around 185s for this model. The total moment is 4.9×10^{22}N-m or M_w9.06.

The fits to the data are shown in Figure 5. Variance reduction is high for the displacements (90%) and somewhat lower (77%) for the velocity time series. The displacement times series are mostly well modeled, the notable exception is at the two northern stations on Hokkaido island HDKH06 and HDKH07 where the amplitude of surface waves arriving between 200 and 300s are underestimated. This is also true for the velocity time series. Additionally, we observe in the velocity time series an underestimation at the higher frequencies. This is obvious for example for stations TCGH10 and IBR008 both in the Kanto region, for the northern stations in Aomori prefecture (AOM004 and AOMG06), and on Hokkaido island (HDKH06 and 07).

The time evolution of slip can be seen in Supplementary animation S1. We include 3 pseudo-rupture fronts in the animation that show the approximate distance a rupture from traveling at 1.5, 2.5 and 3.5km/s would have traveled. In agreement with the source time function of Figure 4b, the rupture starts slowly, propagating both up and down dip. At around 30s the rupture accelerates up dip and expands along strike rapidly reaching peak slip at around 70s. Up dip there is slip of at least 10m on a segment of about 350km in length. Down dip the behavior is very different. There is an initial slip pulse that propagates down from the hypocenter at around 2.5km/s until about 50s and to about 45km depth. This is followed by a second pulse of deep slip starting at about 60s that propagates down from the epicenter and then laterally, very quickly, mostly along-strike to the south. There is very little slip at depths larger than 50km.

Another way to examine the time dependent behavior of rupture is to study the individual source time functions (STFs) of each subfault (Figure 6). Plotted is the moment rate for every subfault with their respective 90% confidence intervals (CIs). The white

lines indicate the lower bounds of the 90% CIs and the grey hatched areas the upper bound. The STFs are colored by pseudo-rupture velocity, which indicates how fast a rupture front would have to travel to each that subfault at a particular instant in time. They are a visual aid to understand the changes in rupture speed in the model. Rupture begins slowly at first but accelerates up dip reaching the the shallowest portions of the model at a pseudo velocity of around 3km/s and spreading along strike. Down dip there seem to be at least two pulses of slip, the second one indicating a very low initial rupture speed down dip from the hypocenter that spreads laterally quite quickly. Another feature present in this plot is the duration of the source time functions. Up dip of the hypocenter rupture durations are long, usually 50s or longer, while down dip the two pulses of slip are closer to 20s each. This makes the up dip STFs very smooth and the deeper ones very peaked suggesting a a depth dependence of the physical properties of the source.

To illustrate the improvements from including velocity as well as displacement data (the DV model) we inverted for a kinematic model using only the seismogeodetic displacements, ignoring the velocity waveforms (henceforth referred to as the D model). The total slip results are shown in Figure S2a. Slip is considerably larger (71m at the trench) while moment is 5.32×10^{19} or $M_w 9.08$ only slightly larger than the DV solution. The peak moment rate for the D model (Figure S2b) is larger at $13 \times 10^{20} Nm/s$, almost 50% more than for the DV solution. Furthermore, while the duration of rupture is similar (180s) peak moment release occurs earlier (65s) with very little moment after 140s. This is best seen in Figure S3 where the two STFs are plotted for comparison. The models are similar up to 50s, then the D model accelerates its moment release quickly to its peak, while the DV model shows a smoother evolution to peak moment release. After the peak, the

ramp-down is similar for both events, but after 100s the D model tapers off to low moment rates very quickly while the DV continues to have significant moment release during the ramp-down. The longer source time function of the DV model is supported by almost all teleseismic inversions [*Shao et al.*, 2011], the low frequency back projection studies [*Kiser and Ishii*, 2012] and hybrid back-projection models that include depth phases [*Yagi et al.*, 2012].

Another view of the differences between the D and DV solutions can be seen in Figure S4. Here we have plotted once more the individual source-time functions for each subfault. Significant differences can be seen. Peak moment rate is 3×10^{19}Nm/s in the DV solution and 5×10^{19}Nm/s in the D solution. Broadly speaking the shapes of the STFs are similar but they are smoother than in the DV solution. There also seem to be some inconsistencies in the timing of rupture. The shallow subfaults (row No.1) have a mixture of fast rupture along strike that has not been reported in other results. Specifically the subfaults at positions 4-6 and 14-17 favor a fast rupture of more than 3 km/s while the central one with the largest moment (Nos. 8-12) favor a slower rupture closer to 2.3 km/s. This behavior of subfaults favoring fast rupture surrounded by slower rupture subfaults is also seen in rows 4 and 5. Down-dip moment is also significantly smaller in the D solution.

These observations, together with the longer total source time function of the DV model, suggest that the net effect of including the velocity waveforms is that they provide improved control on the timing of rupture. In this case, it has the secondary effect of reducing the peak slip from 71 to 52m with a minimal reduction in total moment. The D solution from the Kalman filter still has significant detail and some of the broad features agree with the DV solution. This is important; models derived from low pass filtered

GPS data alone [*Yue and Lay*, 2011] show much less detail in the subfault source-time functions. Furthermore they are fairly insensitive to rupture velocity. *Yue and Lay* [2011] showed that data fits to the GPS data were mostly unchanged when assuming maximum rupture velocities anywhere between 1.5 and 3km/s and even higher. This led them to prefer a model with a maximum rupture speed of 1.5 km/s which we now know from back projection studies [*Wang and Mori*, 2011; *Kiser and Ishii*, 2012] is adequate in the early stages of the rupture but far too slow for the whole event. In fact if we choose such a slow rupture velocity in our inversions the fits to the velocity waveforms are severely degraded. Again, the velocity data provide improved control on the timing of slip, but we recognize that the seismogeodetic displacement-only results still provide a significant improvement over GPS-only solutions.

3.2. Joint Inversion with Tsunami Waveforms

Figure 7 shows the source model after incorporating the 8 wave gauge stations into the inversion (henceforth referred to as the DVT model). Peak slip is now 63m, compared to the 52m from the land-only DV inversion of Figure 4 and moment is 5.51×10^{22}N-m (M_w9.09) compared to 4.89×10^{22}N-m (M_w9.06). The final slip of the DV model (Figure 4) prefers a horizontally symmetric slip distribution about the hypocenter. For the DVT inversion (Figure 7a) slip is 25m or larger for the top 20km of the fault restricted to the south of the hypocenter while north of the hypocenter large slip is confined to the shallowest 10km. There is also noticeable shallowing of peak slip in general with the DVT model having a larger accumulation of shallow slip. The total source time functions (Figure 7b) are very similar. The timing of peak moment rate is delayed in the DVT model from 75 to 80s but its value is unaltered. Furthermore, the DVT has an increase

in moment relative to the land-only DV model at times after peak moment rate although the total duration is similar (190s). A notable difference between both slip inversions are the two patches of 10m of slip on the shallowest portions of both northern and southern extremes. While the DV model does have slip at the edges of the model (about 5m) there is a visible increase of slip in the DVT model. The fits to the wave gauge data are good (VR is 71%, Figure 7c); notably the peak amplitudes at both pressure gauges (OB.TM1 and OB.TM2) are well modeled.

As for the land-based models we can also study the individual subfault source time functions (Figure 8). Recall that plotted is the moment rate for every subfault with their respective 90% confidence intervals. The white lines indicate the lower bounds of the 90% CIs and the grey hatched areas the upper bound of the CI. The STFs are colored by pseudo-rupture velocity, indicating how fast a rupture front would have to travel to each subfault at a particular instant in time. A comparison with the land-based DV solution from (Figure 6) shows that the model is largely unchanged for the subfaults down-dip from the hypocenter. There seem to be at least two pulses of slip. The first one has low peak moment and very short durations. The second pulse propagates down dip from the hypocenter and then spreads laterally quickly; it has longer durations (about 20s) and higher moment rates.

Up dip the behavior in the DVT model using the complete data set is different from the DV model (Figure 6). As we noted in the total slip distribution shown in Figure 7a moment release north of the hypocenter is smaller. More importantly the source time functions are significantly longer for the shallowest 2 rows of subfaults and north of the hypocenter (along strike indices 5-9). In the preferred DV model those shallow source

functions have durations of the order of 50s, while in the DVT inversion the STFs can be as long as 100s, essentially occupying the entire allowed duration. South of the hypocenter on the shallow subfaults, duration of the STFs does not increase as much, but there is a second pulse of slip in the subfaults with largest moment release (along-strike indices 10-12) whose amplitude is larger than for the preferred land-only model. Overall, the effect of including the tsunami wave data is to produce a more pronounced pattern of shallow slip, to shift more of the moment release to the southern half of the slab and to produce longer duration STFs on the shallowest subfaults.

3.3. Tsunami Propagation and Runup Prediction

When employed as an initial condition for tsunami modeling, the DVT kinematic inversion result of Figure 7a, which uses all the available data (seismogeodetic and tsunami wave), has a significant effect on the tsunami intensity and propagation pattern. Figure 9a shows the total vertical deformation including the contribution of the horizontal motion of bathymetry. There is a broad region around the epicenter of long wavelength uplift between zero and about 7m which is largely responsible for the first pulse of tsunami energy observed at the wave gauges (Figure 7c) as a slow and steady increase in sea-surface height. At the frontal part of the continental slope and particularly at the trench there is much larger uplift with shorter wavelength features (up to 22m of uplift). This deformation is associated with the short wavelength high amplitude tsunami peak which is especially visible on stations OB.TM1 and OB.TM2 at 14 and 18 minutes after origin time, respectively. It is interesting to note that both deep slip and shallow slip contribute to tsunamigenesis. It is also important to highlight the contribution of horizontal motion of bathymetry to the uplift pattern. Figure 9b shows the contours of eastward horizontal

displacement predicted at the seafloor and the associated predicted uplift computed using Equation 1. The uplift is largest in the regions of largest horizontal motion and steepest terrain (Figure 3), namely closest to the trench (up to 3m), making this an important contributor to the tsunami initial condition. On the continental shelf, as expected, horizontal motions contribute very little to the vertical deformation pattern. These results agree well with the predictions of *Tanioka and Sataka* [1996] who argued that horizontal motions could account for a significant portion of the tsunamigenic uplift.

The net effect of the improvements to the tsunami propagation model discussed in this section can be seen in Figure 10. Figure 10a shows the maximum tsunami amplitude predicted when using the DVT kinematic inversion as the initial condition. The model predicts large tsunami amplitudes, in excess of 10m along the coast between 37.5°N and 40°N. There are two main lobes of tsunami energy that focus on the Sanriku coast, while amplitudes in Sendai Bay are also large, most likely due to bay resonance effects [*Satake et al.*, 2013]. The model shown in Figure 10b is the result of removing the contribution of horizontal advection of bathymetry from the tsunami's initial condition. The basic propagation pattern is similar but the amplitudes are diminished. Figure 10c shows the maximum amplitude if the kinematic model is applied instantaneously as is usually done with static inversions; it produces a tsunami with a significantly larger amplitude. This will be addressed further on. Finally Figure 10d shows the results from the DV kinematic inversion using seismogeodetic displacement and velocity waveform data (Figure 4). The predicted maximum amplitude pattern is not very different from the DVT model.

A detailed analysis of the small scale runup pattern produced by the different models reveal their capabilities at producing features with high spatial resolution. Figure 11a-d

and Table 1 compare the run ups predicted by the kinematic DV and DVT models with the land-only static source models of *Melgar and Bock* [2013]. The improvement from the kinematic inversion of just land-only data is significant; this model predicts run ups at 1334 of the 2250 survey points compared to only 956 from the static source model. Addition of the tsunami wave gauge data to the inversion further improves the prediction so that 1598 of the 2250 survey points are inundated with 86% variance reduction. Particularly in the full DVT model's prediction, the high runup amplitudes along the southern portion of the Sanriku coast (between 38.4°N and 39.2°N) are well captured. This is an improvement over the static models of *Melgar and Bock* [2013] which had trouble predicting large tsunami amplitudes in some portions of this segment of the coast. The forecast of the northern Sanriku coast is slightly better with more points inundated but we remain unable to model the large runup amplitudes in the narrow valleys. We argued in [*Melgar and Bock*, 2013] that this is due to the limited resolution of the bathymetric data set used here but secondary sources of tsunami energy are a distinct possibility [*Tappin et al.*, 2014]. Furthermore, as shown here, neglecting the horizontal advection of topography greatly diminishes the intensity of the predicted runup (Figure 11d and Table 1). We conclude that the DVT kinematic source model, which includes land and ocean data, provides the best prediction of tsunami runup. We stress again that the land-only kinematic model (DV) is a significant improvement over static dislocation models and provides a reliable source of information for tsunami warnings.

4. Discussion

4.1. Model Resolution and Data Coherence

Each data type, seismogeodetic displacement, velocity and tsunami wave data has different resolving power for the distribution of fault slip. This heterogeneous sensitivity can be seen in Figure 15. Shown are the diagonal values of the resolution matrix. The resolution matrix is expressed as $\mathbf{R} = \mathbf{G}^{\#}\mathbf{G}$ where $\mathbf{G}$ is the expanded Green's function matrix that includes the regularization matrices and regularization weight; $\mathbf{G}^{\#}$ is its generalized inverse [*Aster et al.*, 2013]. If all model parameters are perfectly resolved and can be independently determined then the resolution matrix will be the identity matrix. If the diagonal values are less than one the value of a particular model parameter can be affected by (is not independent of) neighboring model parameters. If the resolution for a particular model parameter is high then that slip value can be considered reliable. A low resolution, on the other hand, indicates that the value of slip is likely the average slip of several neighboring sub-faults. Thus, low resolution is indicative of a smeared out model that cannot resolve sharp features. The resolution matrix indicates that the displacement time series are most sensitive to slip closest to the coast and almost completely insensitive to slip close to the trench; any trench-proximal slip on displacement-only models is likely the result of averaging on deeper faults as well. The velocity time series on the other hand show no along-dip bias. The value of the resolution matrix is similar throughout. That is, velocity data are equally sensitive to slip anywhere on the fault. In turn, the tsunami wave observations are most sensitive to slip by the trench and, in this case, due to the station distribution, to the northern half of the fault model.

Using displacement and velocity waveforms for the same site improves the along-dip resolution of the model; it also has an effect on the timing of rupture. In Section 3.1 we remarked that adding the seismogeodetic velocity waveforms as observations to the inversion provides more detail in the sub-fault source time functions, without degrading the fits to displacement data. This has an impact on the frequency bandwidth of the inversion model considering that the data are low pass filtered at 0.5Hz. Figure 12 shows the coherence between the land-based seismogeodetic data and synthetic waveforms derived from the preferred DVT model. Coherence is typically high at periods longer than 7-8s but we also see bands of high coherence at higher frequencies in both the displacement and velocity data. We attempted to invert data low pass filtered at 1Hz and found that, while the results are not substantially altered, coherence at frequencies higher than 0.5Hz is close to zero. It is quite likely that the degradation in the fits to the data at periods shorter than 7-8s is due to the large spatial discretization of the fault as well as un-modeled Earth structure [*Graves and Wald*, 2001; *Wald and Graves*, 2001]. Thus, one area of immediate improvement might be to use a 3D Earth model for computing the GFs.

4.2. Implications of the Slip Model

The seismogeodetic inversion with displacement and velocity data (DV) provides a broadband image of the source; we can capture both the high frequency features of rupture and the longer period detail. The elevated coherence at higher frequencies previously discussed supports this. Typically, back projection studies are conducted at frequencies higher than 0.5-1.0 Hz. For the 2011 Tohoku-oki event this was the case for the earlier studies [*Wang and Mori*, 2011; *Koper et al.*, 2011]. While the model results shown here

broadly agree with those high frequency source images, it is difficult to defend such an assertion given the different frequency ranges over which these studies image the source. There have been long period back projection studies, particularly *Kiser and Ishii* [2012] (0.05-0.5Hz) and *Yagi et al.* [2012] (0.1-0.5Hz) that we can compare our results against. The comparison shows good agreement. The hybrid back projection of *Yagi et al.* [2012] shows an initial up-dip rupture speed of 3km/s, which is similar to what we find. Down-dip they image a fast (4km/s) pulse of slip followed by a slower one (1.5km/s) that then expands along strike, mostly to the south. Meanwhile *Kiser and Ishii* [2012] do not resolve the initial up-dip slip but do see the slow down dip pulse (0.8km/s), which then rapidly expands laterally to the south at (3.4km/s). We see similar features in the DVT model.

The DVT model is in agreement with longer period observations as well, particularly with the teleseismic model of *Shao et al.* [2011], which uses the wavelet analysis technique of *Ji et al.* [2002]. Such a model assigns equal weights to all frequency components and is not biased by short period body waves or long period surface waves, and is thus easier to compare against. The total slip is similar as is the time evolution of rupture. Additionally we are able to model large amounts of shallow slip, greater than 50 m the top 10 km of the slab, in agreement with seafloor geodetic observations and repeat bathymetry [*Fujiwara et al.*, 2011; *Sato et al.*, 2011].

The joint model can be interpreted within the framework of the depth varying properties of subduction zone megathrusts [*Lay et al.*, 2012]. The megathrust can be divided into 4 domains, domain A which extends from the trench to around 10-15 km depth and experiences either aseismic stable sliding or large coseismic rupture during tsunami events. Domain B then extends down to around 35km and has large total slip while being relatively

depleted of coherent high frequency radiation. Domain C extends from there down to 55km depth and usually has reduced amounts of slip but higher content of short period radiation. Domain D is the transition to stable sliding where slow slip and tremor tend to occur. This is a conceptual model and there is significant variability worldwide. Domain B contains the large asperities while deeper in domain C there are only smaller asperities surrounded by conditionally stable material.

The reason for these differences is varied and disputed; variations in geometry, mineral phases, fault roughness, pore fluids, thermodynamic conditions and rock types likely all contribute [*Heuret et al.*, 2011]. However the conceptual model of [*Lay et al.*, 2012] indicates that whatever the cause, there should be observable differences in the behavior of the fault as depth increases. The 2011 Tohoku event ruptured the three seismogenic domains (A-C). From our source model we can make some interesting observations about the rupture. It nucleates at 21km depth in domain B and after a modest initial phase produces large amounts of moment release in domain A in a steady, smooth fashion. There is evidence of a tsunami event, the 1896 Sanriku earthquake, which ruptured the shallowest part of the northern half of the 2011 Tohoku-oki source region with about 6m of slip [*Tanioka and Sataka*, 1996]. This is significantly smaller than the large slip (50m) we observe in our results. This indicates that the shallow domain A section must be capable of strain accumulation, if only slowly, and is not simply slipping aseismically. It is also possible that dynamic weakening can change the rate and state properties of domain A [*Noda and Lapusta*, 2013] such that it can participate in coseismic rupture. This means that under certain conditions rupture from below can instigate shear failure in the usually creeping shallow section of the megathrust.

If the megathrust properties vary with depth then the nature of rupture should as well [*Lay et al.*, 2012]. Indeed, we can observe such behavior in our model. Figure 13a shows the normalized multi-taper power spectral densities of the slip rate functions from Figure 8. We can see a marked difference between the shallow and deep slip rate spectra. Figure 13b shows the spectra stacked by the along-dip row number. It is clear that the shallow sub faults are depleted in short-period energy. High frequency radiation increases with depth. The width of confidence intervals on the source-time functions (Figure 8) imply that this interpretation must be taken with caution, particularly for the deeper sub faults with smaller moment release. The long, smooth, source time functions with large slip on the shallow parts of the fault could be related to slip on a low friction fault and fast, sharp slip of short duration at depth are likely related to brittle failure on a high friction fault [*Kanamori and Brodsky*, 2004]. Initial results from deep drilled cores suggest a very low coefficient of friction in the shallow megathrust [*Fulton et al.*, 2013].

The introduction of tsunami data into the inversion requires longer source time functions, in agreement with the tsunami-only model of *Satake et al.* [2013], which also requires patches of large slip at the northern and southern extremes. Perhaps the protracted slip durations on the shallow sub faults are aseismic. It is possible that there are unmodeled sources of tsunami energy and that a more physically realistic tsunami source is warranted. For example *Kawamura et al.* [2012] documented compelling evidence from underwater cameras for mass wasting offshore Sanriku. *Arai et al.* [2013] demonstrated from ocean bottom pressure sensor data, heat flow measurements and cores the existence of wide-spread turbidity currents in the northern region of the Tohoku-oki source; these could contribute to tsunamigenesis. Indeed, [*Tappin et al.*, 2014] proposed a submarine

landslide source and modeled its contributions in detail. They found that adding a landslide offshore Sanriku which was delayed 135 s after the onset of rupture to the coseismic source better explains wave gauge and survey data. *Tsuji et al.* [2013] found extensive extensional faulting with measurable vertical motion in the overriding crust landwards of the continental backstop. *Grilli et al.* [2013] showed with 3D finite element modeling that realistic earth structure models can improve models of tsunami generation while *Ma and Hirakawa* [2013] demonstrated that inelastic behavior of the wedge can also significantly alter the vertical deformation pattern of the shallowest portion of the megathrust environment. These phenomena may contribute to the differences between the land-only (DV) and DVT models. Particularly, the northern patch of shallow slip introduced in the inversion which is in a region of adequate resolution (Figure 15), could be a result of the delayed landslide source proposed by *Tappin et al.* [2014]; its location is slightly north of the landslide source proposed by that study but this could be a result of the delayed onset of the landslide being mapped onto a sub fault further from the hypocenter to account for the delay. Nonetheless, and overall it seems that inclusion of tsunami wave data produces a more physically plausible slip pattern with significantly more detail than source models that rely on more limited data types.

4.3. Stress drop and aftershock correlation

The great earthquake on March 11 was followed by a series of normal and thrust fault aftershocks as large as M_w 7.9, so it is informative to correlate aftershock types and locations on the fault interface with changes in stress. Figure 14a shows 6 months of aftershocks occurring within 10km of the slab colored by faulting type superimposed on the stress drop. We employ the *Okada* [1992] method which relies on computation of strain

at each subfault from which the stress is computed based on the physical properties of the medium. To calculate the stress drop we use a homogenous half space approximation [*Lin and Stein*, 2004], although a 1D layered model was assumed for the slip inversion and forward modeling. The aftershocks are from the F-net moment tensor catalogue (http://www.fnet.bosai.go.jp/). We retain only events whose perpendicular distance to the slab model does not exceed 10 km. An aftershock is identified as a thrust event if its strike is similar to the strike of the sub faults in the fault model, between 170° and 230°, its dip between 5° and 30° and its rake is between 70° and 110°; normal faulting aftershocks are those with the same strike and dip as the thrust events but with rake angles between 250° and 290°. To quantify the correlation between stress changes and aftershock type we use a modified version of the Pearson coefficient that measures the correlation between two binary variables. This is known as the Φ coefficient. We find a modest correlation, $\Phi = 0.52$ between normal faulting aftershocks occurring in regions of positive stress drop and thrust events occurring in regions of negative stress drop, where it is expected that the fault surface will be loaded by slip elsewhere. Surprisingly, we see that normal faulting aftershocks occur in regions of large positive stress drop, which is usually associated with a relaxation of stress, but is consistent with arguments of a dynamic overshoot [*Ide et al.*, 2011]. In the case of overshoot, total slip on the shallow portion of the fault exceeds the accumulated tectonic slip deficit and produces normal faulting aftershocks on this portion of shallow dipping megathrust to recover the excess slip. On the other hand, for the DV slip inversion derived from land-based seismogeodetic data (Fig. 14b) there is a negligible correlation between the stress drop pattern and the aftershock distribution ($\Phi = 0.12$). Assuming then that the kinematic inversion using the more diverse data

set is most physically plausible, it may be suitable for operational earthquake forecasting (OEF) aimed to provide probabilistic statements about the likelihood of earthquake occurrence [*Jordan et al.*, 2011]. A better slip inversion can provide a better forecast of aftershock distribution and potential magnitude. The uncertainties are large and reflect a fundamental lack of understanding about short time scale processes, but might be useful during periods of elevated seismicity such as during aftershock sequences following great events, as is this study. OEF can be used to communicate to both government and the public a forecast of time dependent seismic hazards. Any reasonable information even with a large uncertainty is better than none at all, as was poignantly illustrated by the events following the 2009 l'Aquila swarm and mainshock [*Marzocchi et al.*, 2014] where a breakdown in communications between scientists, government and civil society lead to criminal prosecution of seismologists in charge of monitoring. Of course for time scales of weeks to months other sources of data such as teleseismic waveforms and postseismic signals [*Bletery et al.*, 2014] can be added for further refinement of the earthquake source model.

4.4. Tsunami Prediction with Kinematic Slip Models

Accounting for the time-dependent deformation of bathymetry is important in predicting the most accurate tsunami propagation pattern. Our analysis of the overall maximum tsunami amplitude (Fig. 10) indicates that the tsunami prediction is most accurate using the full kinematic earthquake source model with a heterogeneous data set (DVT) as initial conditions to the tsunami model (Figures 10, 11). Often, in tsunami modeling the time dependent deformation of bathymetry is ignored [*MacInnes et al.*, 2013] and kinematic models are assumed to instantly deform the seafloor, i.e. as a static source. If we apply

the kinematic DVT model as a static source and deform the seafloor instantaneously it results in a tsunami with significantly larger maximum amplitude. This discrepancy can be understood by studying Figure 16 where we show snapshots of the first 180 s of tsunami propagation on a trench-perpendicular profile for both cases. Note that the final seafloor deformation is the same, i.e. they both reach the same static field. The key difference is that for the kinematic initial condition we observe a smoother transition from the rest state to the uplift of the sea surface. The tsunami propagation speed is $\sqrt{g}h$ where g is the acceleration due to gravity and h is the water depth so that water depths of 3000-8000 m between the shelf break and the trench yield propagation velocities of 10 to 17 km/min. Thus, there is ample time during the approximately 3 minutes of source duration for the tsunami waves to propagate away from their particular source loci and interfere with tsunami waves being generated elsewhere. This also explains why at basin-wide distances considering a kinematic versus a static source has little impact on propagation modeling [*Fujii and Satake*, 2007]; as time progresses the differences between the two become smaller. Static source models will not always produce larger tsunami amplitudes. If static tsunami GFs are employed [*Romano et al.*, 2012; *Melgar and Bock*, 2013], similar maximum expected amplitudes are obtained. The inversion procedure adjusts by placing spurious slip elsewhere on the slab in order to account for the observed time series at the wave gauges. The key point is that if a tsunami modeler uses a kinematic earthquake source model as an initial conditions to study near-field tsunami propagation [*MacInnes et al.*, 2013] and applies it as a static one, i.e. deforms the sea-floor instantaneously, they will most likely obtain larger amplitudes than if using the correct temporal evolution of deformation.

Additionally, Figure 10d shows the maximum expected tsunami amplitude using the DV model as the initial conditions. The pattern is similar, but the maximum amplitude is generally smaller. This is not surprising considering the full kinematic model places more slip at the trench than the land-only model. However, our results demonstrate that even if wave gauges are unavailable a kinematic earthquake source model derived from near-source land-based seismogeodetic observations provides a much improved estimate of the tsunami intensity compared to the static model.

As demonstrated for the 2011 Tohoku-oki event, our tsunami runup prediction compared to ground truth indicates that tsunami intensity can be extracted in considerable detail (Figure 11). Tsunami intensity maps can be extracted from the model output for any region of interest. The scale of these maps is inherently limited by the discretization of the topography and bathymetry data sets. If a certain application requires more detail then it will be necessary to use finer data sets, as provided, for example, by lidar and multi-beam surveys. In Figure 17 and animations S2-S6 we show an example for Sendai Bay where inundation distances were long [*Mori et al.*, 2012], often of the order of kilometers. The snapshot at zero minutes shows the initial configuration of the coastline as defined by the SRTM3 and SRTM30+ topography and bathymetry data sets. At 45 minutes the main tsunami waves enter the bay; at 60 minutes runup commences on the northern portion of the bay. The main wavefront then arrives at the central and southern shoreline. At 80 minutes there is significant runup along the entire coastline of the bay with inundation distances of the scale of kilometers. We can observe detailed wave structure as the runup channels up valleys and rivers. The blue dots in the snapshots are the locations of the survey points from [*Mori et al.*, 2012], the model inundates 891 out of 1023 points in this

portion of the domain with 89% variance reduction. We can observe that the general runup pattern matches well the distribution of survey points in agreement with the high variance reduction of the tsunami model. The importance of the post-event surveys for our conclusions cannot be overstated; they provide the ground truth and are critical for correct assessment of our earthquake source model and resulting tsunami prediction model, irrespective of the approach or data types used. With adequate planning and selection of target areas it should be possible to produce runup maps like these for key areas (such as nuclear power plants) where a detailed prediction of runup is required to make emergency response decisions.

It is also important to note that a robust system that attempts to provide information about tsunami intensity must rely on diverse data sets. There is compelling observational and modeling evidence that a secondary tsunami source in the form of an underwater landslide contributes to the large runups in the northern Sanriku region [*Tappin et al.*, 2014]. While we cannot directly model such a source in this approach, by using tsunami wave measurements some of that complexity may be absorbed as extra detail in the kinematic inversion. As discussed in Section 4.1 this might explain the northern patch of shallow slip. This is a nuisance for source analysis but also results in the tsunami intensity being better modeled than when using on-shore data alone (Figure 8). Thus by relying on multiple geophysical measurements the algorithm is less prone to gross underestimates of tsunami intensity.

We can also see from Figure 17 that there is significant structure to the tsunami in the open waters of the bay. We have not discussed other physical variables in this work but quantities such as flow speed are often more important for infrastructure such as

ports and harbors [*Lynett et al.*, 2014] than the tsunami amplitude. It is possible to incorporate them into the tsunami model with the same techniques discussed here. There are still significant improvements to be made. We have assumed with both static and kinematic source models that the water column responds instantaneously to the vertical motion of the sea floor. Realistically there is a finite time over which the deformation of the sea floor is transferred to the sea surface. This can be modeled as a superposition of acoustic waves [*Ohmachi et al.*, 2001], but there are few studies that take this into account and the magnitude of the error incurred is unclear. *Ohmachi et al.* [2001] suggests, for example, that significant tsunamigenic potential that amplify the sea surface height can occur when the natural acoustic period of the sea water layer, which depends exclusively on depth, is close to that of the oceanic Rayleigh waves. At higher frequencies *Kozdon and Dunham* [2014] have shown that acoustic waves might reflect important characteristics of the shallow source. Future studies should include this extra source term and quantify its importance. As far as runup is concerned, by using the depth-averaged shallow water equations we are neglecting vertical flow velocities [*Lynett*, 2006]. We have also not accounted for the entrainment of sediments into the flow[*Simpson and Castelltort*, 2006]. Both of these assumptions may need to be relaxed for achieving meter-scale predictions of tsunami runup.

4.5. Suitability for Rapid Implementation

We have presented here a retrospective analysis of available geophysical data for the 2011 M_w9.0 Tohoku-oki earthquake. A valid question is whether tsunami prediction can be automated and performed in now time. Seismic and GPS data are routinely collected with sub-second latencies. Permanent ocean bottom observatories such as the

ones used here (TM1 and TM2) are cabled and telemetered in real time. Data retrieval from moored GPS buoys relies on real-time satellite telemetry, which may be less robust. In any case, data retrieval should introduce latencies of no longer than a few seconds, at which time analysis can begin. The source inversion procedure is designed as a multi-tiered algorithm. First, the faulting type and location of the dislocation surfaces must be surmised. Outer rise events such as the 2009 Mw 8.1 Samoa earthquake [*Okal et al.*, 2010] and the 2012 Mw8.6 Wharton Basin strike-slip event [*Meng et al.*, 2012] off-shore Sumatra underscore the inadequacy of assuming a priori faulting types and geometries for a large earthquake. However, with the availability of regional geodetic data it is possible to calculate the faulting type and likely dislocation surface [*Melgar et al.*, 2013b; *Minson et al.*, 2014]. This computation is straightforward and should not add significant latency *Grapenthin et al.* [2014]. Kinematic source modeling, as shown here, can be performed immediately after the faulting geometry is determined, provided GFs have been pre-computed. Even if several tens to a few hundred inversions are necessary to determine the optimal smoothing to be applied, the computational overhead is not significant. Once the kinematic model is available the tsunami prediction can be initiated, and with suitable computer code parallelization should be available within a few minutes. The model can then be updated as tsunami wave data, with lower latencies than seismic and geodetic data, are accumulated [*Melgar and Bock*, 2013]. This indirect approach to warning is still susceptible to tsunamis generated by non-seismic sources such as underwater landslides, although it can be coupled with traditional tsunami warning algorithms that can trigger on disturbances recorded at off-shore stations [*Tsushima et al.*, 2014]. Furthermore not all geophysical networks are as dense as those in Japan. For implementation in a given region

it will be important to assess what level of detail and reliability can be expected from the runup predictions given the number and type of sensors available. Through diversity of data types and instrument locations it is reasonable to expect detailed predictions of tsunami intensity immediately following the onset of large seismic ruptures.

5. Conclusions

We have shown by retrospective real-time analysis of the 2011 Tohoku-oki event that rapid near-source earthquake source modeling and tsunami prediction restricted to strong-motion accelerometer data that are subject to systematic errors (baseline offsets) are significantly enhanced by the addition of high-rate geodetic data, by providing real-time seismogeodetic displacement and velocity waveforms. Further improvement is obtained by supplementing land-based data with off-shore measurements of the ensuing tsunami waves, including seafloor pressure sensors and GPS-equipped buoys. The kinematic source models thus obtained are consistent with conceptual models of subduction zone properties. They exhibit depth dependent behavior that was quantified through frequency domain analysis of the slip rate functions. The stress drop distribution is also found to be significantly more correlated with aftershock locations and mechanism types when off-shore tsunami wave data are included. We also showed that the kinematic models can be used as initial conditions for predictions of tsunami wave runup. We included the horizontal advection of steeply sloping bathymetric features into the tsunamigenic budget. Comparison with post-event tsunami survey measurements showed that we have achieved reliable predictions of tsunami inundation and runup. We conclude that through data diversity it should be possible with careful algorithm design, to produce reliable now-time kinematic slip inversions and tsunami runup predictions in near source coastal regions most susceptible

to loss of life and damage to critical infrastructure within minutes of rupture initiation regardless of earthquake magnitude and faulting mechanism

Acknowledgments. This research was funded by the NASA Earth and Space Science Fellowship NNX12AN55H, and NASA AIST-11 NNX09AI67G and ROSES NNX12AK24G awards. We'd like to thank Randy LeVeque for discussions on tsunami modeling and Doug Dreger for helpful comments on kinematic slip inversion. We extend our thanks to the National Research Institute for Earth Science and Disaster Prevention for access to accelerometer data (http://www.kyoshin.bosai.go.jp/); the Geospatial Information Authority for access to GPS data, the Earthquake Research Institute for access to ocean-bottom pressure data (http://www.jamstec.go.jp/scdc/top_e.html), and the Nationwide Ocean Wave information network for GPS buoy data (http://nowphas.mlit.go.jp/info eng.html). Kalman filtering routines are available at http://github.com/dmelgarm/pykal and the kinematic inversion code is available at http://github.com/dmelgarm/Mudpy. GeoClaw is available from the developers at http://www.clawpack.org. We are thankful for a constructive review from an anonymous reviewer.

References

Akaike, H. (1980), Likelihood and the Bayes procedure, *Trabajos de estadística y de investigación operativa*, *31*(1), 143–166.

Allen, R. M., P. Gasparini, O. Kamigaichi, and M. Böse (2009), The status of earthquake early warning around the world: an introductory overview, *Seismological Research Letters*, *80*(5), 682–693.

Arai, K., H. Naruse, R. Miura, K. Kawamura, R. Hino, Y. Ito, D. Inazu, M. Yokokawa, N. Izumi, and M. Murayama (2013), Tsunami-generated turbidity current of the 2011 Tohoku-oki earthquake, *Geology*, *41*(11), 1195–1198.

Aster, R. C., B. Borchers, and C. H. Thurber (2013), *Parameter estimation and inverse problems*, Academic Press.

Berger, M. J., D. L. George, R. J. LeVeque, and K. T. Mandli (2011), The GeoClaw software for depth-averaged flows with adaptive refinement, *Advances in Water Resources*, *34*(9), 1195–1206.

Beroza, G. C., and P. Spudich (1988), Linearized inversion for fault rupture behavior: Application to the 1984 Morgan Hill, California, earthquake, *Journal of Geophysical Research*, *93*(B6), 6275–6296.

Bletery, Q., A. Sladen, B. Delouis, M. Vallée, J.-M. Nocquet, L. Rolland, and J. Jiang (2014), A detailed source model for the mw9. 0 tohoku-oki earthquake reconciling geodesy, seismology and tsunami records, *Journal of Geophysical Research: Solid Earth*.

Bock, Y., D. Melgar, and B. W. Crowell (2011), Real-time strong-motion broadband displacements from collocated GPS and accelerometers, *Bulletin of the Seismological Society of America*, *101*(6), 2904–2925.

Boore, D. M., and J. J. Bommer (2005), Processing of strong-motion accelerograms: needs, options and consequences, *Soil Dynamics and Earthquake Engineering*, *25*(2), 93–115.

Boore, D. M., C. D. Stephens, and W. B. Joyner (2002), Comments on baseline correction of digital strong-motion data: Examples from the 1999 Hector Mine, California, earthquake, *Bulletin of the Seismological Society of America*, *92*(4), 1543–1560.

Brown, H. M., R. M. Allen, M. Hellweg, O. Khainovski, D. Neuhauser, and A. Souf (2011), Development of the ElarmS methodology for earthquake early warning: Realtime application in California and offline testing in Japan, *Soil Dynamics and Earthquake Engineering*, *31*(2), 188–200.

Brune, J. N. (1970), Tectonic stress and the spectra of seismic shear waves from earthquakes, *Journal of Geophysical Research*, *75*(26), 4997–5009.

Colombelli, S., R. M. Allen, and A. Zollo (2013), Application of real-time GPS to earthquake early warning in subduction and strike-slip environments, *Journal of Geophysical Research*, *118*(7), 3448–3461.

Crowell, B. W., Y. Bock, and D. Melgar (2012), Real?time inversion of GPS data for finite fault modeling and rapid hazard assessment, *Geophysical Research Letters*, *39*(9).

Crowell, B. W., D. Melgar, Y. Bock, J. S. Haase, and J. Geng (2013), Earthquake magnitude scaling using seismogeodetic data, *Geophysical Research Letters*.

Emore, G. L., J. S. Haase, K. Choi, K. M. Larson, and A. Yamagiwa (2007), Recovering seismic displacements through combined use of 1Hz GPS and strong-motion accelerometers, *Bulletin of the Seismological Society of America*, *97*(2), 357–378.

Farr, T. G., P. A. Rosen, E. Caro, R. Crippen, R. Duren, S. Hensley, M. Kobrick, M. Paller, E. Rodriguez, and L. Roth (2007), The shuttle radar topography mission, *Reviews of*

geophysics, *45*(2).

Fujii, Y., and K. Satake (2007), Tsunami source of the 2004 sumatra–andaman earthquake inferred from tide gauge and satellite data, *Bulletin of the Seismological Society of America*, *97*(1A), S192–S207.

Fujii, Y., and K. Satake (2013), Slip distribution and seismic moment of the 2010 and 1960 chilean earthquakes inferred from tsunami waveforms and coastal geodetic data, *Pure and Applied Geophysics*, *170*(9-10), 1493–1509.

Fujiwara, T., S. Kodaira, T. No, Y. Kaiho, N. Takahashi, and Y. Kaneda (2011), The 2011 Tohoku-oki earthquake: Displacement reaching the trench axis, *Science*, *334*(6060), 1240–1240.

Fukahata, Y., Y. Yagi, and M. Matsu'ura (2003), Waveform inversion for seismic source processes using ABIC with two sorts of prior constraints: Comparison between proper and improper formulations, *Geophysical Research Letters*, *30*(6).

Fukuyama, E., M. Ishida, D. Dreger, and H. Kawai (1998), Automated seismic moment tensor determination by using on-line broadband seismic waveforms, *J. Seismol. Soc. Jpn*, *51*, 149–156.

Fulton, P., E. Brodsky, Y. Kano, J. Mori, F. Chester, T. Ishikawa, R. Harris, W. Lin, N. Eguchi, and S. Toczko (2013), Low coseismic friction on the Tohoku-oki fault determined from temperature measurements, *Science*, *342*(6163), 1214–1217.

Genrich, J. F., and Y. Bock (2006), Instantaneous geodetic positioning with 10–50 Hz GPS measurements: Noise characteristics and implications for monitoring networks, *Journal of Geophysical Research*, *111*(B3).

George, D. L. (2008), Augmented Riemann solvers for the shallow water equations over variable topography with steady states and inundation, *Journal of Computational Physics*, *227*(6), 3089–3113.

George, D. L., and R. J. LeVeque (2006), Finite volume methods and adaptive refinement for global tsunami propagation and local inundation., *Science of Tsunami Hazards*, *24*(5), 319.

Gonzalez, F., R. LeVeque, P. Chamberlain, B. Hirai, J. Varkovitzky, and D. George (2011), Geoclaw results for the NTHMP tsunami benchmark problems, in *Proceedings and Results of the 2011 NTHMP Model Benchmarking Workshop*.

González, F. I., E. N. Bernard, C. Meinig, M. C. Eble, H. O. Mofjeld, and S. Stalin (2005), The NTHMP tsunameter network, *Natural Hazards*, *35*(1), 25–39.

Grapenthin, R., I. A. Johanson, and R. M. Allen (2014), Operational real-time gps-enhanced earthquake early warning, *Journal of Geophysical Research: Solid Earth*, *119*(10), 7944–7965.

Graves, R. W., and D. J. Wald (2001), Resolution analysis of finite fault source inversion using one-and three-dimensional Green's functions: 1. strong motions, *Journal of Geophysical Research*, *106*(B5), 8745–8766.

Grilli, S. T., J. C. Harris, T. S. T. Bakhsh, T. L. Masterlark, C. Kyriakopoulos, J. T. Kirby, and F. Shi (2013), Numerical simulation of the 2011 Tohoku tsunami based on a new transient FEM co-seismic source: Comparison to far-and near-field observations, *Pure and Applied Geophysics*, *170*(6-8), 1333–1359.

Gusman, A. R., Y. Tanioka, B. T. MacInnes, and H. Tsushima (2014), A methodology for near-field tsunami inundation forecasting: Application to the 2011 tohoku tsunami,

Journal of Geophysical Research: Solid Earth.

Hartzell, S. H., and T. H. Heaton (1983), Inversion of strong ground motion and teleseismic waveform data for the fault rupture history of the 1979 Imperial Valley, California, earthquake, *Bulletin of the Seismological Society of America*, *73*(6A), 1553–1583.

Haskell, N. (1964), Total energy and energy spectral density of elastic wave radiation from propagating faults, *Bulletin of the Seismological Society of America*, *54*(6A), 1811–1841.

Hayes, G. P., P. S. Earle, H. M. Benz, D. J. Wald, and R. W. Briggs (2011), 88 hours: The US Geological Survey National Earthquake Information Center response to the 11 March 2011 Mw 9.0 Tohoku earthquake, *Seismological Research Letters*, *82*(4), 481–493.

Hayes, G. P., D. J. Wald, and R. L. Johnson (2012), Slab1.0: A three-dimensional model of global subduction zone geometries, *Journal of Geophysical Research*, *117*(B1).

Heuret, A., S. Lallemand, F. Funiciello, C. Piromallo, and C. Faccenna (2011), Physical characteristics of subduction interface type seismogenic zones revisited, *Geochemistry, Geophysics, Geosystems*, *12*(1).

Hoshiba, M., and T. Ozaki (2014), Earthquake early warning and tsunami warning of the japan meteorological agency, and their performance in the 2011 off the pacific coast of tohoku earthquake, in *Early Warning for Geological Disasters*, edited by F. Wenzel and J. Zschau, Advanced Technologies in Earth Sciences, pp. 1–28, Springer Berlin Heidelberg.

Ide, S., M. Takeo, and Y. Yoshida (1996), Source process of the 1995 Kobe earthquake: Determination of spatio-temporal slip distribution by Bayesian modeling, *Bulletin of the Seismological society of America*, *86*(3), 547–566.

Ide, S., A. Baltay, and G. C. Beroza (2011), Shallow dynamic overshoot and energetic deep rupture in the 2011 mw 9.0 tohoku-oki earthquake, *Science*, *332*(6036), 1426–1429.

Jaiswal, K. S., and D. J. Wald (2010), Development of a semi-empirical loss model within the USGS prompt assessment of global earthquakes for response (PAGER) system, in *Proceedings of the 9th US and 10th Canadian conference on earthquake engineering: reaching beyond borders*, pp. 25–29.

Ji, C., D. J. Wald, and D. V. Helmberger (2002), Source description of the 1999 Hector Mine, California, earthquake, part I: Wavelet domain inversion theory and resolution analysis, *Bulletin of the Seismological Society of America*, *92*(4), 1192–1207.

Ji, C., D. V. Helmberger, D. J. Wald, and K.-F. Ma (2003), Slip history and dynamic implications of the 1999 Chi-Chi, Taiwan, earthquake, *Journal of Geophysical Research*, *108*(B9).

Jordan, T. H., Y.-T. Chen, P. Gasparini, R. Madariaga, I. Main, W. Marzocchi, G. Papadopoulos, G. Sobolev, K. Yamaoka, and J. Zschau (2011), Operational earthquake forecasting. state of knowledge and guidelines for utilization, *Annals of Geophysics*, *54*(4).

Kanamori, H., and E. E. Brodsky (2004), The physics of earthquakes, *Reports on Progress in Physics*, *67*(8), 1429.

Kawamura, K., T. Sasaki, T. Kanamatsu, A. Sakaguchi, and Y. Ogawa (2012), Large submarine landslides in the Japan Trench: A new scenario for additional tsunami generation, *Geophysical Research Letters*, *39*(5).

Kiser, E., and M. Ishii (2012), The March 11, 2011 Tohoku-oki earthquake and cascading failure of the plate interface, *Geophysical Research Letters*, *39*(7).

Koper, K. D., A. R. Hutko, T. Lay, C. J. Ammon, and H. Kanamori (2011), Frequency-dependent rupture process of the 2011 Mw 9. 0 Tohoku earthquake: Comparison of short-period p wave backprojection images and broadband seismic rupture models, *Earth, planets and space*, *63*(7), 599–602.

Kozdon, J. E., and E. M. Dunham (2014), Constraining shallow slip and tsunami excitation in megathrust ruptures using seismic and ocean acoustic waves recorded on ocean-bottom sensor networks, *Earth and Planetary Science Letters*, *396*, 56–65.

Lay, T., H. Kanamori, C. J. Ammon, K. D. Koper, A. R. Hutko, L. Ye, H. Yue, and T. M. Rushing (2012), Depth-varying rupture properties of subduction zone megathrust faults, *Journal of Geophysical Research*, *117*(B4).

LeVeque, R. J. (2002), *Finite volume methods for hyperbolic problems*, vol. 31, Cambridge university press.

LeVeque, R. J., D. L. George, and M. J. Berger (2011), Tsunami modelling with adaptively refined finite volume methods, *Acta Numerica*, *20*(1), 211–289.

Lin, J., and R. S. Stein (2004), Stress triggering in thrust and subduction earthquakes and stress interaction between the southern san andreas and nearby thrust and strike-slip faults, *Journal of Geophysical Research: Solid Earth (1978–2012)*, *109*(B2).

Lynett, P. J. (2006), Nearshore wave modeling with high-order boussinesq-type equations, *Journal of Waterway, Port, Coastal, and Ocean engineering*, *132*(5), 348–357.

Lynett, P. J., J. Borrero, S. Son, R. Wilson, and K. Miller (2014), Assessment of the tsunami-induced current hazard, *Geophysical Research Letters*, *41*(6), 2048–2055.

Ma, S., and E. T. Hirakawa (2013), Dynamic wedge failure reveals anomalous energy radiation of shallow subduction earthquakes, *Earth and Planetary Science Letters*, *375*,

113–122.

MacInnes, B. T., A. R. Gusman, R. J. LeVeque, and Y. Tanioka (2013), Comparison of earthquake source models for the 2011 Tohoku event using tsunami simulations and near-field observations, *Bulletin of the Seismological Society of America*, *103*(2B), 1256–1274.

Marzocchi, W., A. M. Lombardi, and E. Casarotti (2014), The establishment of an operational earthquake forecasting system in italy, *Seismological Research Letters*, *85*(5), 961–969.

Melgar, D. (2014), *Seismogeodesy and Rapid Earthquake and Tsunami Source Assessment*, 247 pp., University of California San Diego, Ph.D. Dissertation.

Melgar, D., and Y. Bock (2013), Near-field tsunami models with rapid earthquake source inversions from land-and ocean-based observations: The potential for forecast and warning, *Journal of Geophysical Research: Solid Earth*, *118*(11), 5939–5955.

Melgar, D., Y. Bock, and B. W. Crowell (2012), Real-time centroid moment tensor determination for large earthquakes from local and regional displacement records, *Geophysical Journal International*, *188*(2), 703–718.

Melgar, D., Y. Bock, D. Sanchez, and B. W. Crowell (2013a), On robust and reliable automated baseline corrections for strong motion seismology, *Journal of Geophysical Research: Solid Earth*, *118*(3), 1177–1187.

Melgar, D., B. W. Crowell, Y. Bock, and J. S. Haase (2013b), Rapid modeling of the 2011 mw 9.0 tohoku-oki earthquake with seismogeodesy, *Geophysical Research Letters*, *40*(12), 2963–2968.

Meng, L., J.-P. Ampuero, J. Stock, Z. Duputel, Y. Luo, and V. Tsai (2012), Earthquake in a maze: compressional rupture branching during the 2012 mw 8.6 sumatra earthquake, *Science*, *337*(6095), 724–726.

Minson, S., J. R. Murray, J. O. Langbein, and J. S. Gomberg (2014), Real-time inversions for finite fault slip models and rupture geometry based on high-rate GPS data, *Journal of Geophysical Research*, *119*(4), 3201–3231.

Mori, N., T. Takahashi, and T. . T. E. T. J. S. Group (2012), Nationwide post event survey and analysis of the 2011 Tohoku earthquake tsunami, *Coastal Engineering Journal*, *54*(01).

Mungov, G., M. Eblé, and R. Bouchard (2013), Dart® tsunameter retrospective and real-time data: A reflection on 10 years of processing in support of tsunami research and operations, *Pure and Applied Geophysics*, *170*(9-10), 1369–1384.

Noda, H., and N. Lapusta (2013), Stable creeping fault segments can become destructive as a result of dynamic weakening, *Nature*, *493*(7433), 518–521.

Ohmachi, T., H. Tsukiyama, and H. Matsumoto (2001), Simulation of tsunami induced by dynamic displacement of seabed due to seismic faulting, *Bulletin of the Seismological Society of America*, *91*(6), 1898–1909.

Okada, Y. (1992), Internal deformation due to shear and tensile faults in a half-space, *Bulletin of the Seismological Society of America*, *82*(2), 1018–1040.

Okal, E. A., H. M. Fritz, C. E. Synolakis, J. C. Borrero, R. Weiss, P. J. Lynett, V. V. Titov, S. Foteinis, B. E. Jaffe, and P. L.-F. Liu (2010), Field survey of the Samoa tsunami of 29 September 2009, *Seismological Research Letters*, *81*(4), 577–591.

Olson, E. L., and R. M. Allen (2005), The deterministic nature of earthquake rupture, *Nature*, *438*(7065), 212–215.

Ozaki, T. (2011), Outline of the 2011 off the Pacific coast of Tohoku earthquake (Mw 9. 0)-tsunami warnings/advisories and observations, *Earth, planets and space*, *63*(7), 827–830.

Romano, F., A. Piatanesi, S. Lorito, N. D'Agostino, K. Hirata, S. Atzori, Y. Yamazaki, and M. Cocco (2012), Clues from joint inversion of tsunami and geodetic data of the 2011 Tohoku-oki earthquake, *Scientific reports*, *2*.

Rydelek, P., and S. Horiuchi (2006), Earth science: Is earthquake rupture deterministic?, *Nature*, *442*(7100), E5–E6.

Sandwell, D. T., and W. H. Smith (2009), Global marine gravity from retracked Geosat and ERS-1 altimetry: Ridge segmentation versus spreading rate, *Journal of Geophysical Research*, *114*.

Satake, K., Y. Fujii, T. Harada, and Y. Namegaya (2013), Time and space distribution of coseismic slip of the 2011 Tohoku earthquake as inferred from tsunami waveform data, *Bulletin of the Seismological Society of America*, *103*(2B), 1473–1492.

Sato, M., T. Ishikawa, N. Ujihara, S. Yoshida, M. Fujita, M. Mochizuki, and A. Asada (2011), Displacement above the hypocenter of the 2011 Tohoku-oki earthquake, *Science*, *332*(6036), 1395–1395.

Shao, G., X. Li, C. Ji, and T. Maeda (2011), Focal mechanism and slip history of the 2011 Mw 9.1 off the Pacific coast of Tohoku earthquake, constrained with teleseismic body and surface waves, *Earth, planets and space*, *63*(7), 559–564.

Simpson, G., and S. Castelltort (2006), Coupled model of surface water flow, sediment transport and morphological evolution, *Computers & Geosciences*, *32*(10), 1600–1614.

Smyth, A., and M. Wu (2007), Multi-rate Kalman filtering for the data fusion of displacement and acceleration response measurements in dynamic system monitoring, *Mechanical Systems and Signal Processing*, *21*(2), 706–723.

Suzuki, W., S. Aoi, H. Sekiguchi, and T. Kunugi (2011), Rupture process of the 2011 Tohoku-oki mega-thrust earthquake (M9. 0) inverted from strong-motion data, *Geophysical Research Letters*, *38*(7).

Tanioka, Y., and L. J. Ruff (1997), Source time functions, *Seismological Research Letters*, *68*(3), 386–400.

Tanioka, Y., and K. Sataka (1996), Fault parameters of the 1896 Sanriku tsunami earthquake estimated from tsunami numerical modeling, *Geophysical Research Letters*, *23*(13), 1549–1552.

Tappin, D. R., S. T. Grilli, J. C. Harris, R. J. Geller, T. Masterlark, J. T. Kirby, F. Shi, G. Ma, K. Thingbaijam, and P. M. Mai (2014), Did a submarine landslide contribute to the 2011 tohoku tsunami?, *Marine Geology*, *357*, 344–361.

Tatehata, H. (1997), The new tsunami warning system of the Japan meteorological agency, in *Perspectives on Tsunami Hazard Reduction*, pp. 175–188, Springer.

Titov, V. V., F. I. Gonzalez, E. Bernard, M. C. Eble, H. O. Mofjeld, J. C. Newman, and A. J. Venturato (2005), Real-time tsunami forecasting: Challenges and solutions, in *Developing Tsunami-Resilient Communities*, pp. 41–58, Springer.

Trifunac, M. (1974), A three-dimensional dislocation model for the San Fernando, California, earthquake of February 9, 1971, *Bulletin of the Seismological Society of America*,

64(1), 149–172.

Trifunac, M. D., and M. I. Todorovska (2001), A note on the useable dynamic range of accelerographs recording translation, *Soil Dynamics and Earthquake Engineering*, *21*(4), 275 – 286.

Tsuda, K., J. Steidl, R. Archuleta, and D. Assimaki (2006), Site-response estimation for the 2003 Miyagi-oki earthquake sequence considering nonlinear site response, *Bulletin of the Seismological Society of America*, *96*(4A), 1474–1482.

Tsuji, T., K. Kawamura, T. Kanamatsu, T. Kasaya, K. Fujikura, Y. Ito, T. Tsuru, and M. Kinoshita (2013), Extension of continental crust by anelastic deformation during the 2011 Tohoku-oki earthquake: The role of extensional faulting in the generation of a great tsunami, *Earth and Planetary Science Letters*, *364*, 44–58.

Tsuruoka, H., H. Kawakatsu, and T. Urabe (2009), GRiD MT (grid-based real-time determination of moment tensors) monitoring the long-period seismic wavefield, *Physics of the Earth and Planetary Interiors*, *175*(1), 8–16.

Tsushima, H., R. Hino, Y. Ohta, T. Iinuma, and S. Miura (2014), tfish/rapid: Rapid improvement of near-field tsunami forecasting based on offshore tsunami data by incorporating onshore gnss data, *Geophysical Research Letters*.

Wald, D. J., and R. W. Graves (2001), Resolution analysis of finite fault source inversion using one-and three-dimensional Green's functions: 2. Combining seismic and geodetic data, *Journal of Geophysical Research*, *106*(B5), 8767–8788.

Wald, D. J., V. Quitoriano, T. H. Heaton, H. Kanamori, C. W. Scrivner, and C. B. Worden (1999), Trinet "shakemaps": Rapid generation of peak ground motion and intensity maps for earthquakes in southern california, *Earthquake Spectra*, *15*(3), 537–

555.

Wang, D., and J. Mori (2011), Rupture process of the 2011 off the Pacific coast of Tohoku earthquake(Mw 9. 0) as imaged with back-projection of teleseismic P-waves, *Earth Planets and Space*, *63*(7), 603.

Yagi, Y., A. Nakao, and A. Kasahara (2012), Smooth and rapid slip near the Japan trench during the 2011 Tohoku-oki earthquake revealed by a hybrid back-projection method, *Earth and Planetary Science Letters*, *355*, 94–101.

Yue, H., and T. Lay (2011), Inversion of high-rate (1 sps) GPS data for rupture process of the 11 March 2011 Tohoku earthquake (mw 9.1), *Geophysical Research Letters*, *38*(7).

Zhu, L., and L. A. Rivera (2002), A note on the dynamic and static displacements from a point source in multilayered media, *Geophysical Journal International*, *148*(3), 619–627.

Table 1. Forecast statistics of the inversions and runup models. The first column is variance reduction of the modeled runup compared to the surveyed runup from *Mori et al.* [2012]. The 2nd column is the number of runup survey points inundated by the model.

Model	Survey VR(%)	Survey Points Inundated
Static, land-only	85	956/2250
Kinematic, land-only	87	1334/2250
Kinematic, land+ocean	86	1598/2250
Kinematic, land+ocean, no horizontal	85	1209/2250

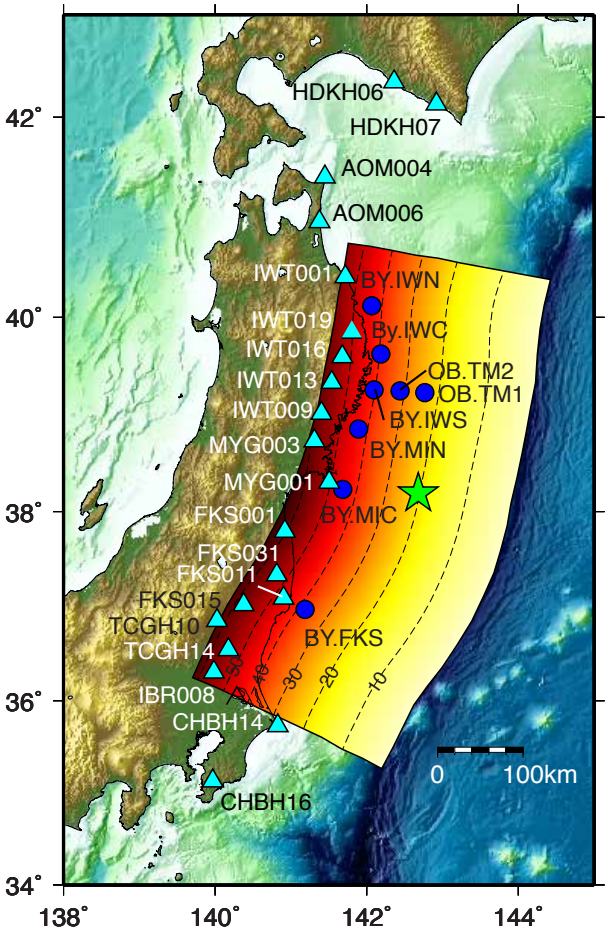

Figure 1. Map of 20 stations seismogeodetic (triangles) and 8 offshore (circles) stations used in the slip inversion. The green star denotes the epicenter. The slab geometry used for the inversion is from *Hayes et al.* [2012] and the contours are depth to the slab in kilometers.

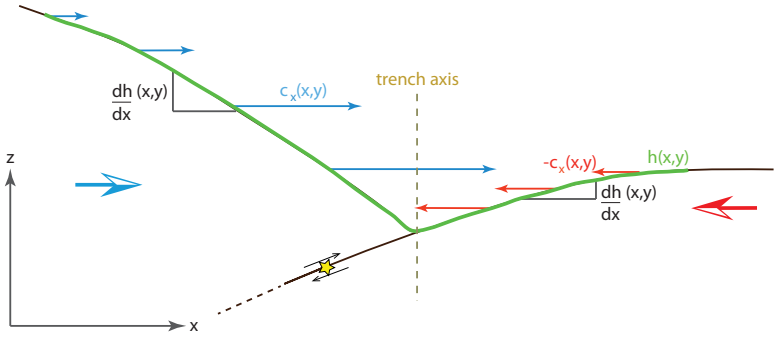

Figure 2. Schematic of tsunami generation from horizontal coseismic motion $c_x(x, y)$ and $h(x, y)$ describes the topography of the seafloor.

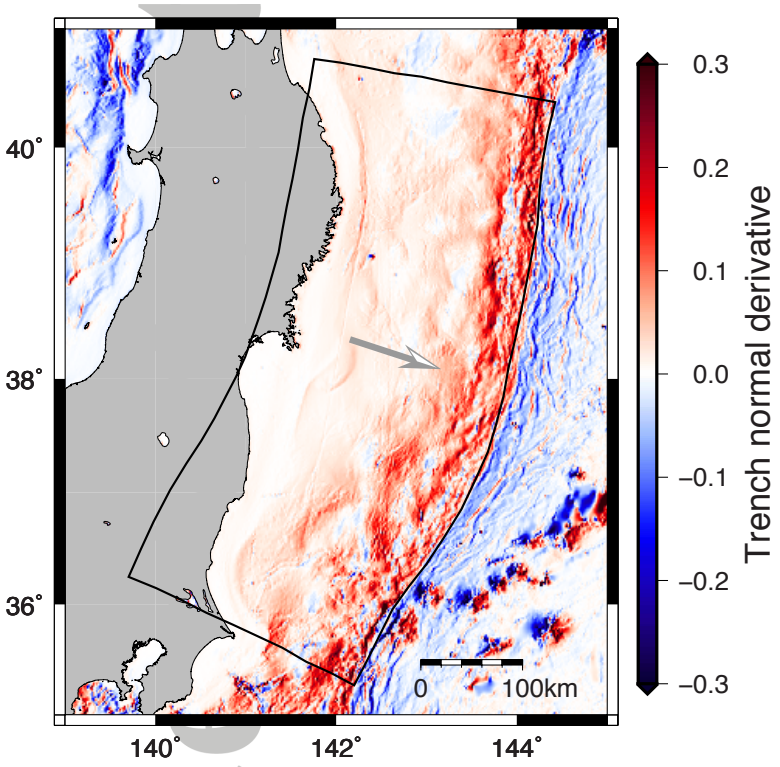

Figure 3. Trench normal derivative of bathymetry computed in the direction indicated by the grey arrow. The black outline is that of the fault model used for the inversion.

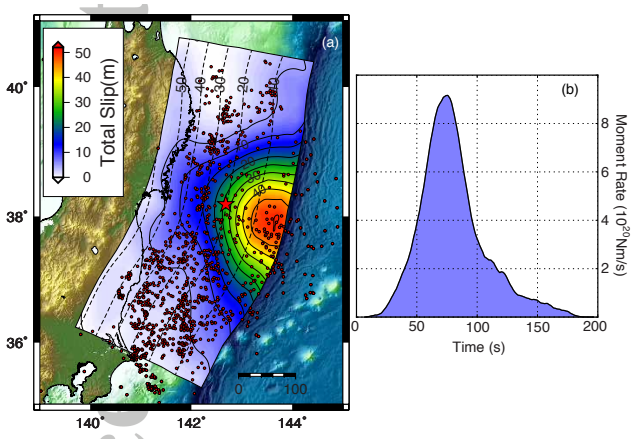

Figure 4. (a) Total slip from the kinematic inversion of seismogeodetic displacement and velocity data (model DV); peak slip is 52m. The red star is the epicenter and the red circles are two weeks of aftershocks from the NIED catalogue. Slip is contoured every 10m and the slab depths are contoured every 10km in dotted lines. (b) The source time function for the kinematic model.

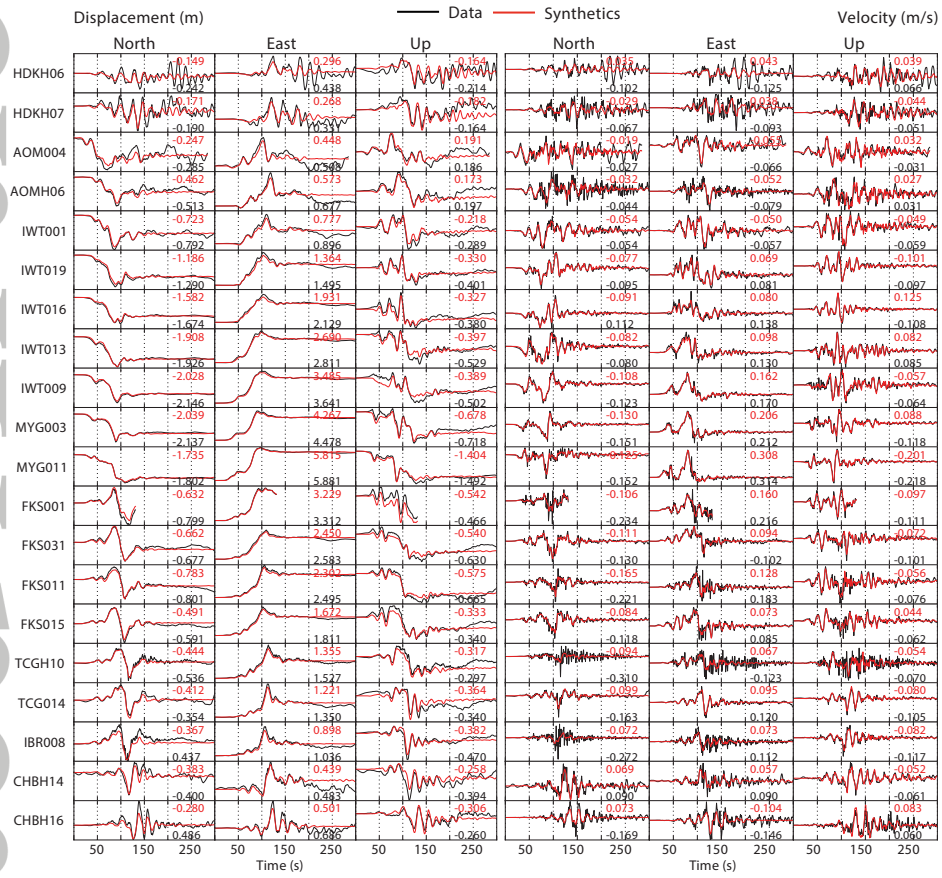

Figure 5. Comparison between observed (black) and synthetic (red) 3-component displacement and velocity time series for model DV. The stations are sorted by latitude from north to south (see Figure 1). The numbers next to the time series represent the value of peak displacement or velocity.

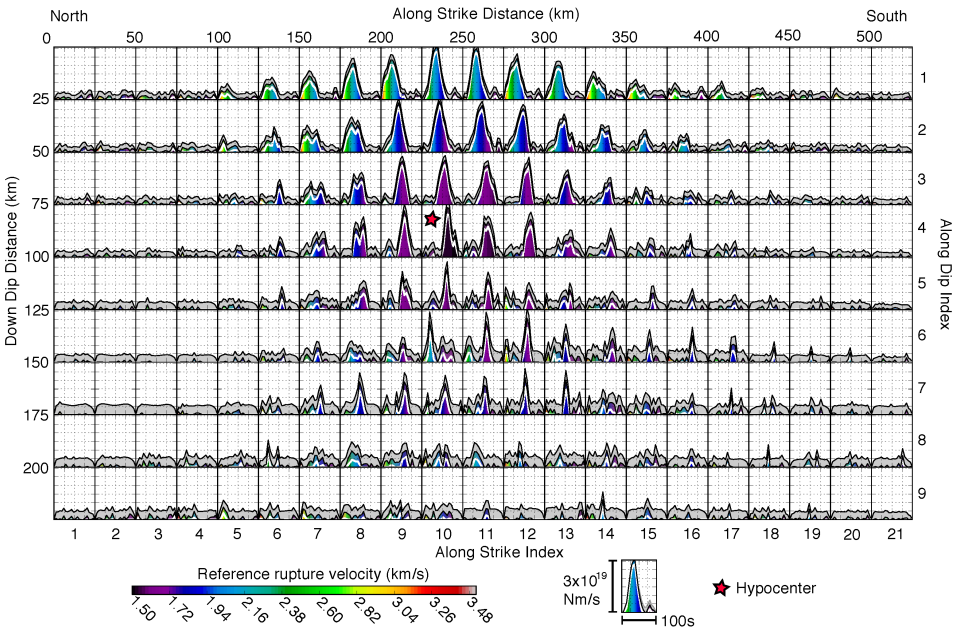

Figure 6. Subfault source-time functions (STFs) for model DV. The 90% confidence intervals are indicated by the white line and the solid grey hatched area. The coloring under the STFs represents the pseudo rupture velocity. The red star indicates the hypocenter. All STFs are plotted at the same scale. The position of the sub fault is given by its down-dip and along strike distance, the along strike and along dip indices indicate the sub fault numbers used for bookkeeping in the inversion. Each sub fault STF starts at the time when the rupture front traveling outwards from the hypocenter at 3.5km/s reaches one of its edges and lasts for 100s after that.

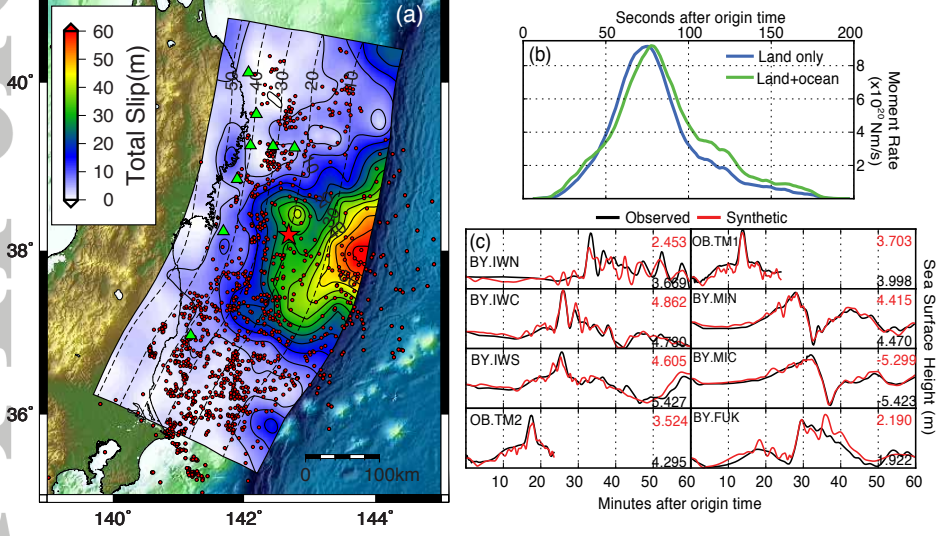

Figure 7. Joint land- and ocean-based data inversion results (model DVT). (a) Preferred result from the inversion incorporating the 8 tsunami wave gauge stations denoted by triangles. Red dots are 2 weeks of aftershocks and the star is the hypocenter. Slip is contoured every 5m and depths to the slab every 10km. (b) Comparison between the source time functions of the seismogeodetic-only inversion (model DV) of Figure 4 and the joint inversion. (c) Fits to the wave gauge data. The black lines are the observed and the red the synthetics. The numbers denote peak amplitudes.

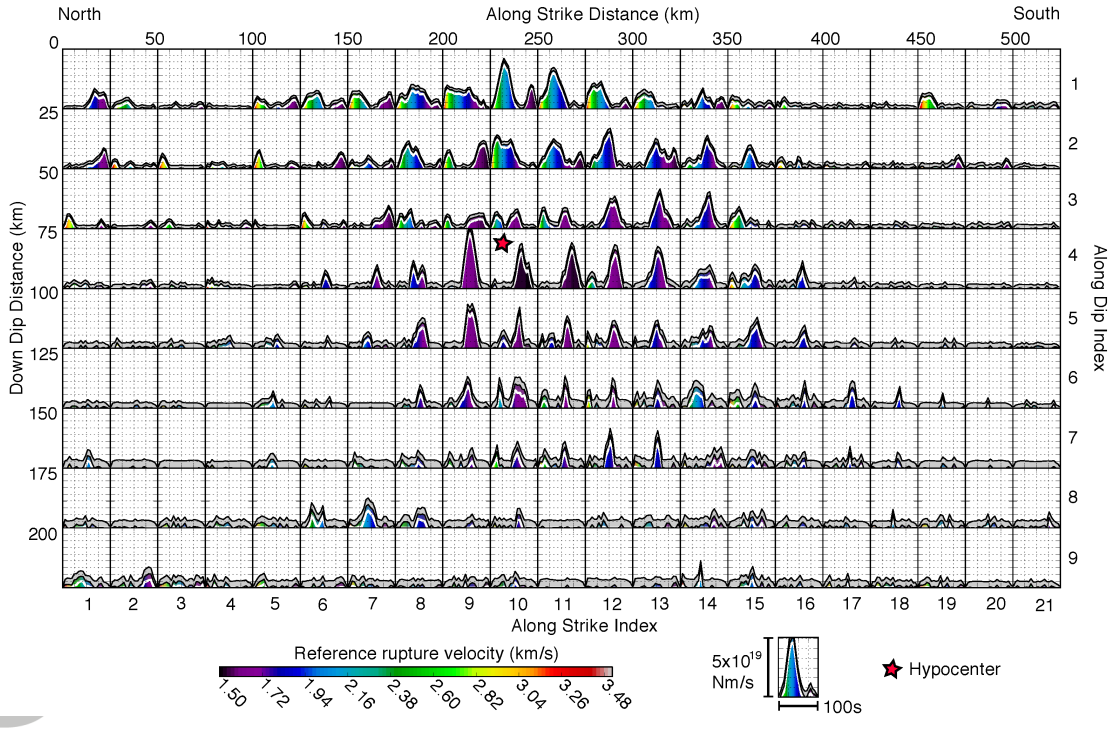

Figure 8. Subfault source-time functions (STFs) for model DVT. The 90% confidence intervals are indicated by the white line and the solid grey hatched area. The coloring under the STFs represents the pseudo rupture velocity. The red star indicates the hypocenter. All STFs are plotted at the same scale.

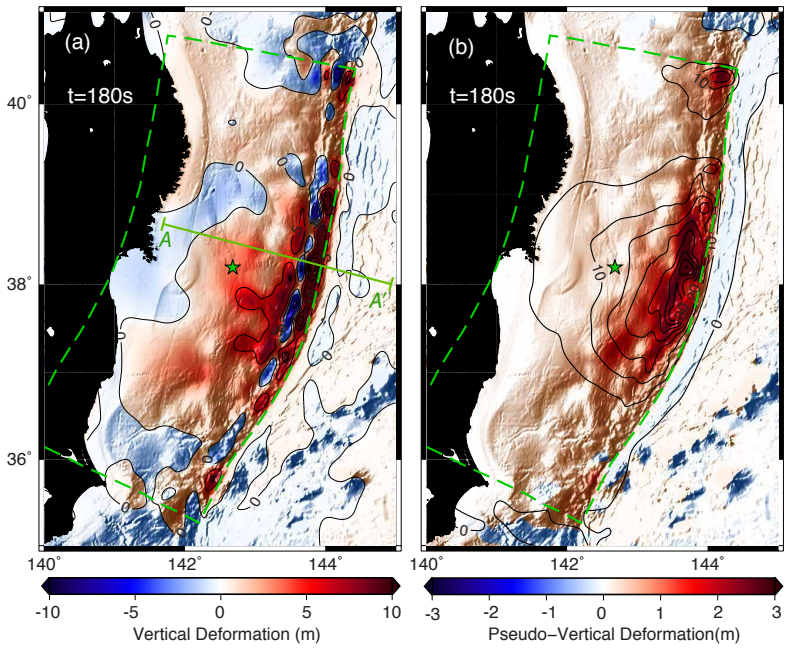

Figure 9. Vertical deformation predicted by the joint slip inversion at t=180s after origin time. (a) Total vertical deformation including effects from horizontal motion of sloping bathymetry. Contours are every 5m, the green star is the epicenter and the green box is the outline of the fault model. The profile A-A' is used later on in Figure (b) Contribution to vertical deformation exclusively from the horizontal motion of the sloping bathymetry. The contours are the eastward horizontal deformation predicted by the slip inversion.

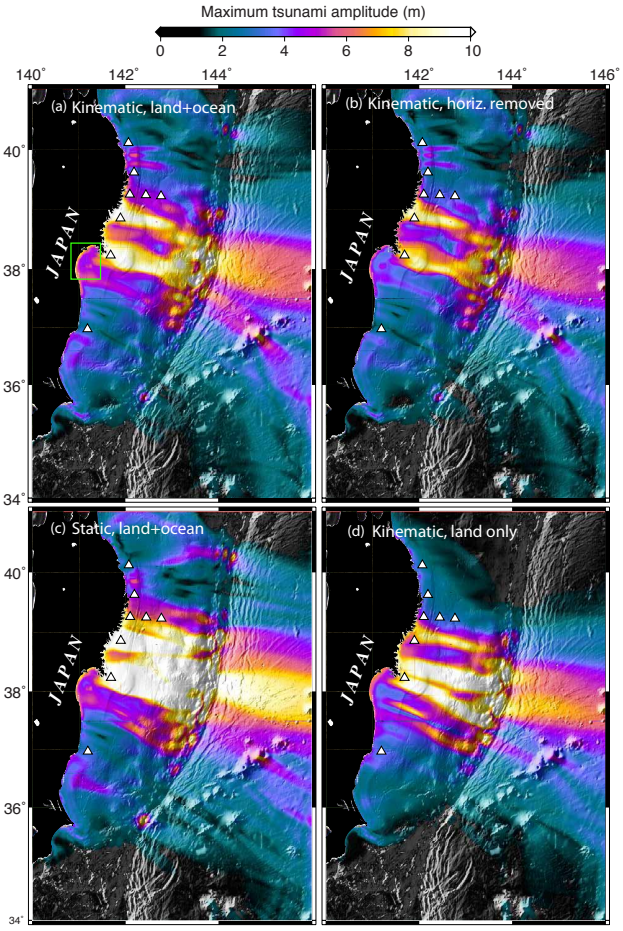

Figure 10. Maximum tsunami amplitudes with several source models. (a) Kinematic joint inversion of land- and ocean-based data (model DVT). The green rectangle is the area used in Animation S2 (b) Model DVT with the contributions of the horizontal motion of bathymetry removed. (c) Model DVT applied instantaneously as a static model. (d) Model DV resulting from the land-based only kinematic inversion of Figure 4.

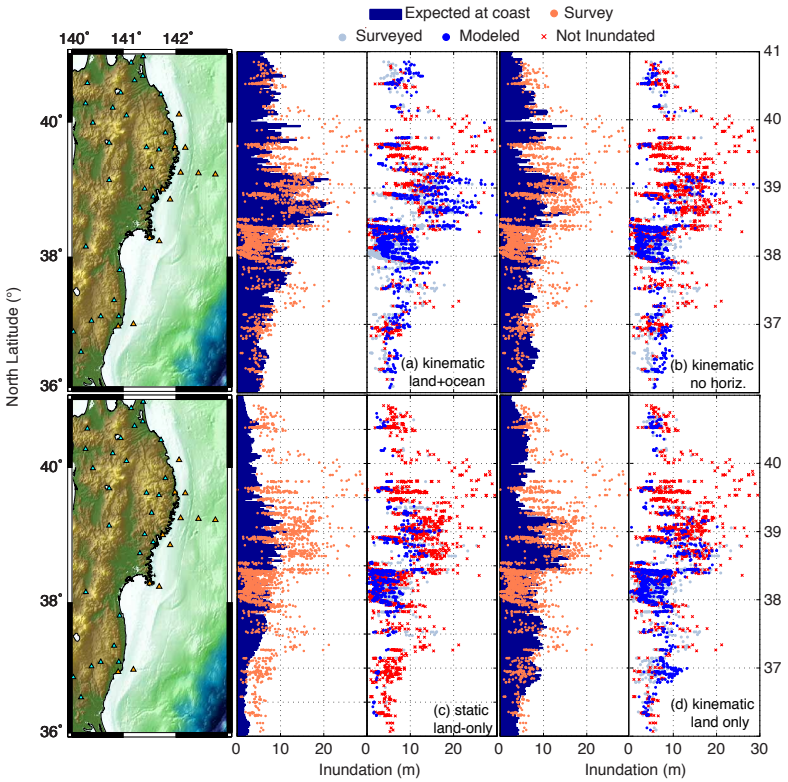

Figure 11. Runup modeling for different slip inversions. The left side of each of the four model panels shows, with blue bars, the flow depth predicted by the model at the coastline (the pre-tsunami land-water boundary) compared to the surveyed runup inland (orange dots) of *Mori et al.* [2012]. The right side of each of the four model panels shows the direct comparison between the observed survey runup (grey dots) and the flow depth plus topography predicted by the model at the survey points (blue dots). The red crosses are survey points that were not inundated by the model. (a) Runup forecast results for the full land and ocean kinematic inversion (model DVT). (b) Runup forecast results for model DVT without the contribution of horizontal topographic advection. (c) Runup forecast result with the static land-only inversion of *Melgar and Bock* [2013](d) Runup forecast results for the land-only DV kinematic inversion.

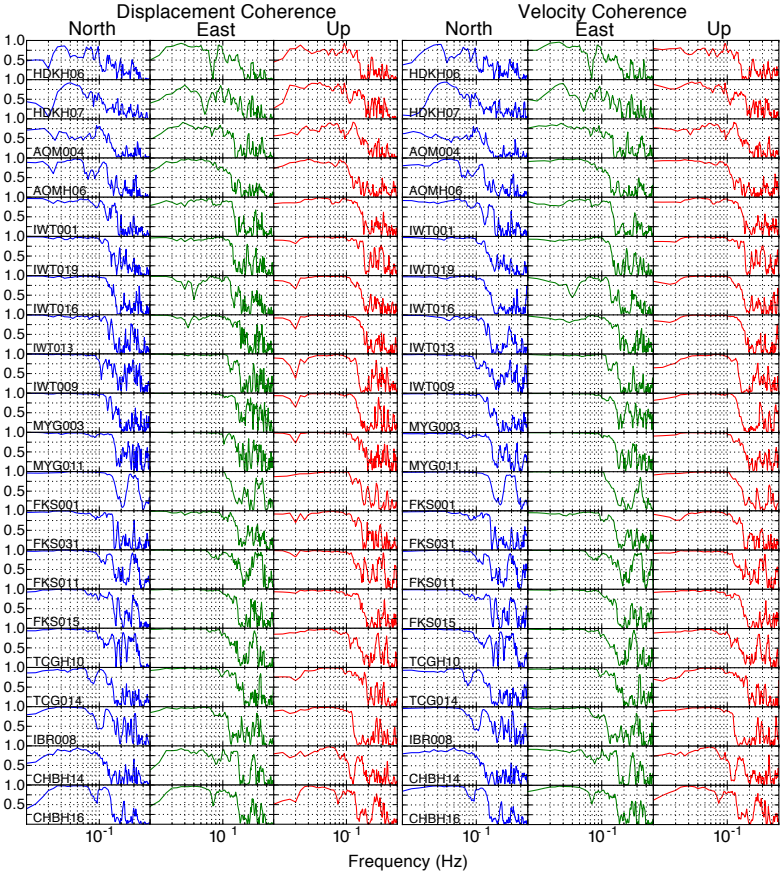

Figure 12. Coherence between 100s and 0.5Hz between observed and synthetic data for the joint DVT inversion results. The stations are sorted from north to south (Figure 1).

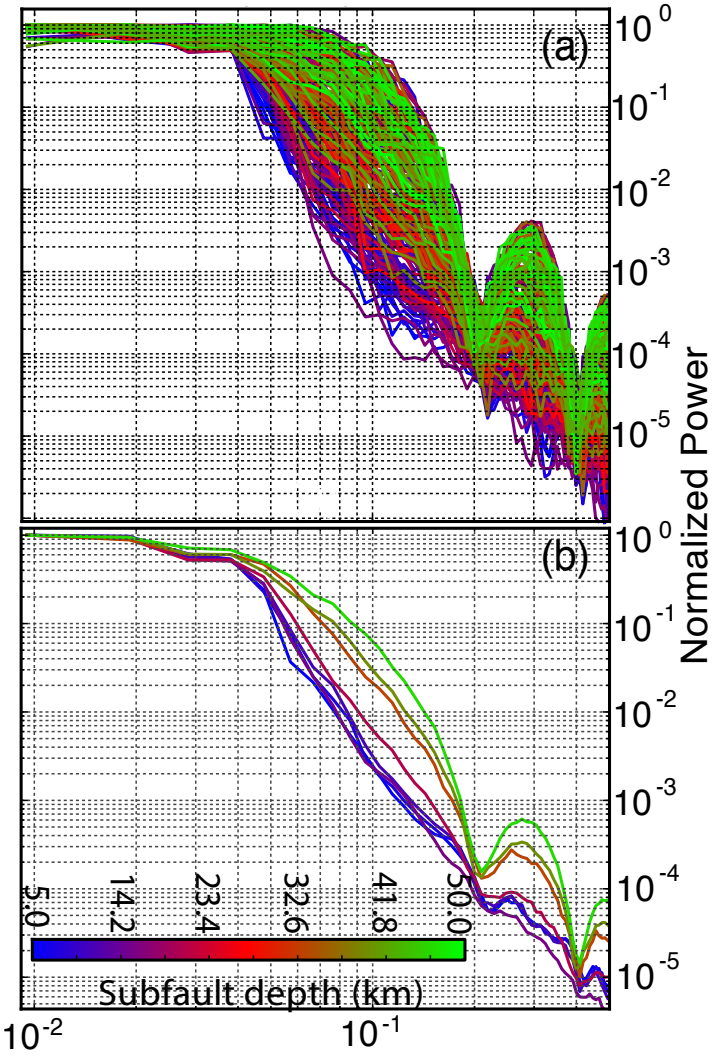

Figure 13. (a)Normalized power spectral densities for the slip rate functions of all sub faults shown in Figure 8.(b) Normalized stacked PSDs for the sub fault source time functions. The spectra are stacked per down-dip row of the model and the color corresponds to their average depth.

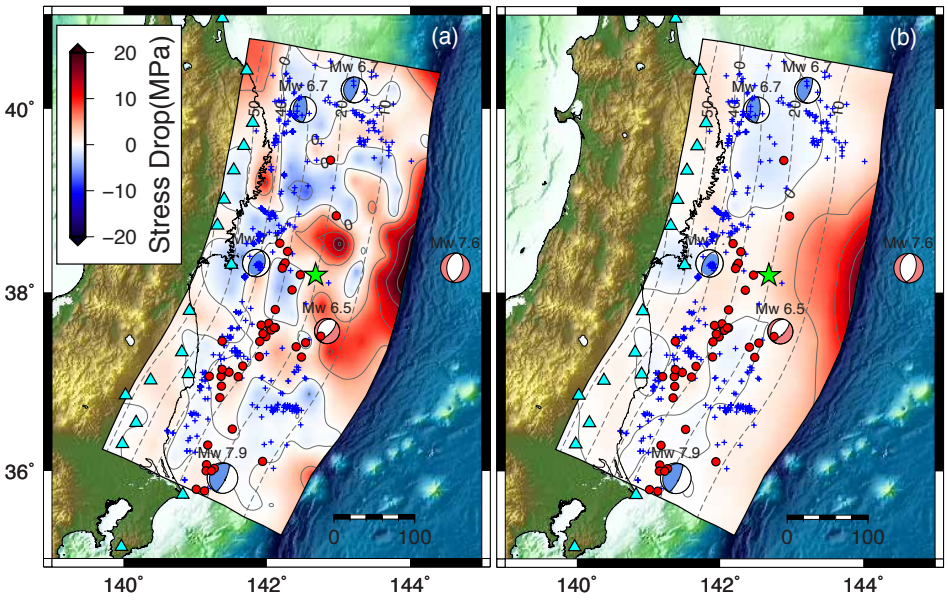

Figure 14. (a) Stress drop for the joint DVT slip inversion in Figure 7 and its correlation with 6 months of aftershocks occurring within 10km of the slab model and with similar strike and dip. Red circles denote normal faulting aftershocks and blue crosses thrust faulting aftershocks. The beach balls indicate notable aftershocks with magnitude larger than M_w6.5. The green star is the hypocenter and the blue triangles are the on-land stations used in the inversion. The dotted lines are the 10km depth contours to the slab model *Hayes et al.* [2012] (b) Same but for the land-only DV kinematic slip inversion.

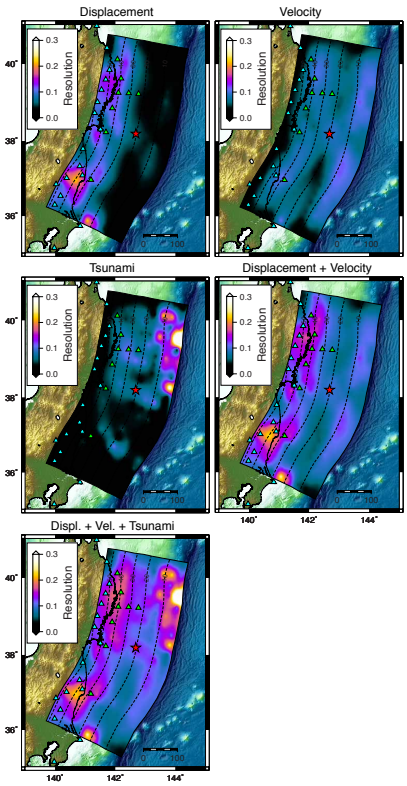

Figure 15. Diagonal values of the resolution matrix. The resolution matrix is expressed as $\mathbf{R} = \mathbf{G}^{\#}\mathbf{G}$ where $\mathbf{G}$ is the expanded Green's function matrix that includes the regularization matrices and regularization weight. $\mathbf{G}^{\#}$ is the generalized inverse [*Aster et al.*, 2013]. This plot highlights the sensitivity of the different data sets to different portions of the subduction geometry, see text for details.

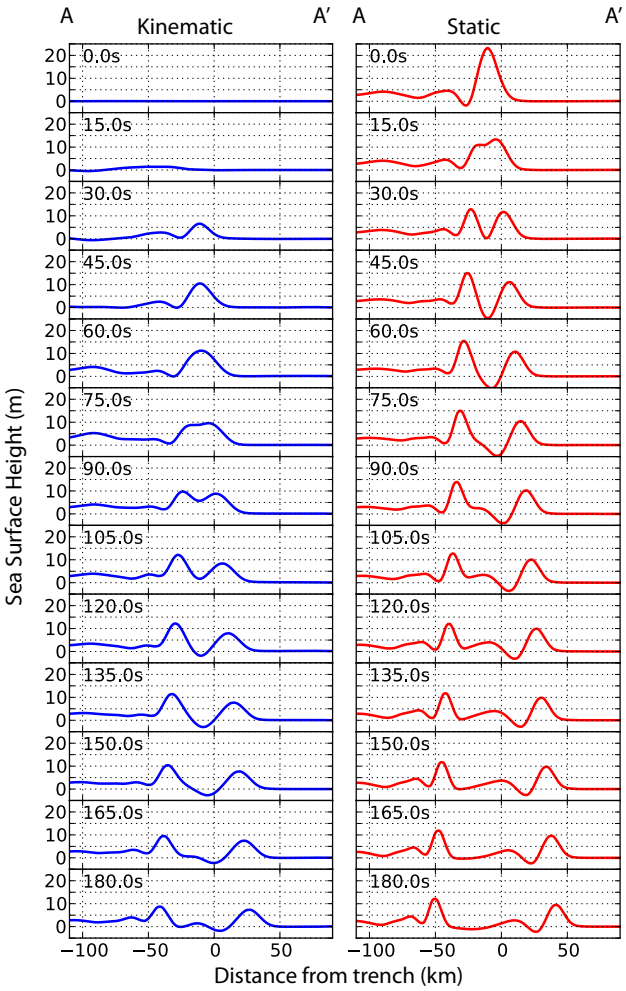

Figure 16. Trench perpendicular profile of tsunami propagation along profile A-A' (Figure 9). Shown are snapshots of the first 180s of tsunami propagation for (left) model DVT applied as a kinematic initial condition and (right) model DVT applied as a static initial condition.

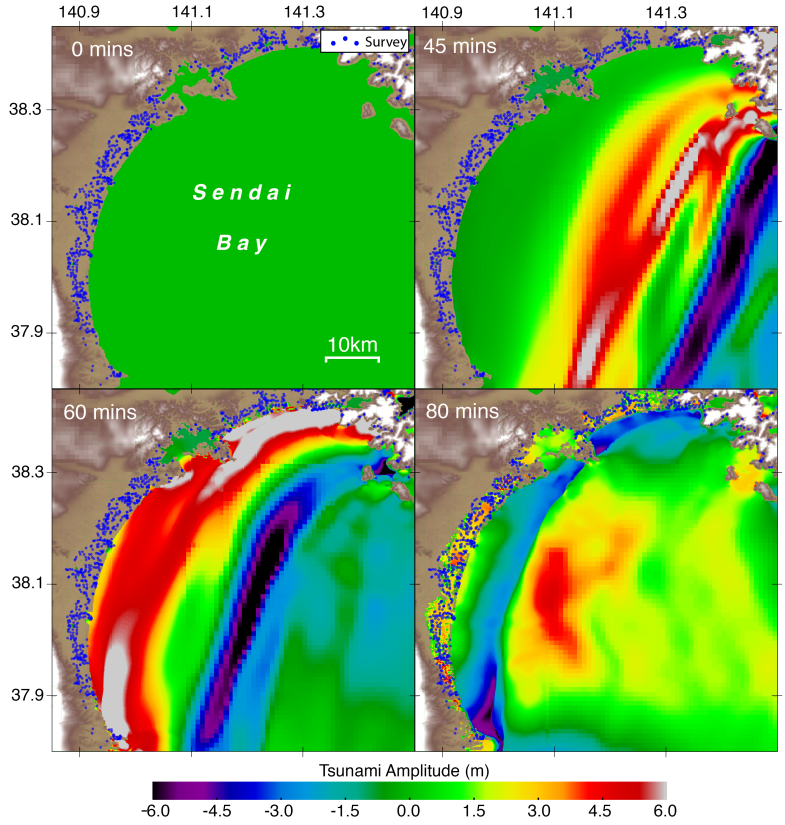

Figure 17. Four snapshots in time of runup modeling of the coast surrounding an area of Sendai Bay outlined in Figure 10a. The tsunami amplitude refers to sea surface height for a tsunami over the ocean and flow depth for a tsunami over land. The blue dots are the locations of the survey measurements from *Mori et al.* [2012]. The model inundates 891 out of 1023 points in this portion of the domain with 89% variance reduction